THESIS

MEASURING SEISMIC ANISOTROPY IN THE MANTLE WEDGE OF JAPAN'S SUBDUCTION SYSTEM USING SHEAR WAVE SPLITTING OF SKS AND SKKS WAVES

Submitted by

Jamie Pierce

Department of Geosciences

In partial fulfillment of the requirements

For the Degree of Master of Science

Colorado State University

Fort Collins, Colorado

Summer 2014

Master's Committee:

Advisor: Derek Schutt

Jay Breidt
Sven Egenhoff
Joe Elkins
Dennis Harry

ABSTRACT

MEASURING SEISMIC ANISOTROPY IN THE MANTLE WEDGE OF JAPAN'S SUBDUCTION SYSTEM USING SHEAR WAVE SPLITTING OF SKS AND SKKS WAVES

Mantle flow patterns can provide a better understanding of mantle deformation and composition in subduction systems. These flow patterns can be inferred by measuring seismic anisotropy. Previous anisotropy studies of Japan's subduction system have found complex fast axis polarizations. Here we seek to better constrain fast axis directions through shear wave splitting of SKS and SKKS waves from events with magnitudes greater than 6.5. Data were collected from the Japanese National Research Institute for Earth Science and Disaster Preventions (NIED) F-net array for stations located over all of Japan. Results from shear wave splitting measurements show trench-parallel fast axes trends near the Ryukyu and Japan Trenches and trench-perpendicular fast axes further away from these trenches. Fast axes near the Nankai Trough align with the subducted plate motion. The Kuril Trench fast axes are roughly perpendicular to subducted plate motion. A simple 2D corner flow model can explain the flow of the mantle wedge if B-type olivine deformation, indicative of hydrated asthenosphere under high stress, is the source of the fast axes perpendicular to mantle flow direction near the Ryukyu Trench, Japan Trench, and Kuril Trench.

ACKNOWLEDGMENTS

The data used in this study was obtained from Japan's National Research Institute for Earth Science and Disaster Prevention's F-net seismic array. The event information was obtained through Standing Order for Data (SOD) [*Owens et al.*, 2004]. Several figures used in the project were plotted using the Taup Toolkit [*Crotwell et al.*, 1999] and the Generic Mapping Tools [*Wessel et al.*, 2013]. Seismic Analysis Code (SAC) was used for aspects of the data processing [*Goldstein et al.*, 2003; *Goldstein and Snoke*, 2005]. [1]

I would like to express my sincerest gratitude to my advisor, Derek Schutt, who through his vast knowledge and experience was able to open the world of geophysics to me. His expertise, encouragement, and patience made the completion of this project possible. I would also like to thank Dennis Harry, Sven Egenhoff, Joe Elkins, and Jay Breidt for serving on my committee and their guidance throughout the project. I would like to thank the faculty and graduate students at Colorado State University's Department of Geoscience for sharing their knowledge and support along the way. Lastly, I would like to thank Ron Millikan for helping me as I struggled through some of the programming, for his help with graphics, and for his overall support. Funding for this project was provided through a Graduate Teaching Assistantship from Colorado Sate University.

[1] Reference lists of citations in this section can be found in Chapter 1 and Chapter 2 where figures and programs were used.

TABLE OF CONTENTS

LIST OF TABLES

LIST OF FIGURES

CHAPTER 1

INTRODUCTION

1.1 Organization of Thesis

This thesis is organized into three chapters. This first chapter contains a broader introduction and explanation of processes than described in Chapter 2. Chapter 2 is written as a technical paper, which will be submitted to a peer reviewed journal that is yet to be determined. The final chapter discusses recommendations for future work.

1.2 Introduction

1.2.1 Mantle Anisotropy

Anisotropy implies a directional dependence to a property (Figure 1.1). In the case of seismology, parts of the earth have a directional dependence in seismic velocity. This seismic velocity anisotropy is often simply termed anisotropy when used in a seismology context and this convention will be used here. Anisotropy is primarily thought to be located in the upper part of the mantle, particularly in the asthenosphere and lithosphere due to the alignment of olivine crystals [*Silver* 1996]. Anisotropy is also located in the inner core, the D” region and the crust [*Long and Becker,* 2010]. Since the D” region is located in the lower mantle, for any given event, anisotropy due to the D” region will be constant for all stations. Any variance of anisotropy detected with nearby stations must occur at much shallower depths then the D” region [*Alsina and Snieder*, 1995]. This study focuses on the anisotropy at shallow depths and not in the D” region.

In the upper mantle, anisotropy is formed by past or present strain, and hence anisotropy measurements can offer a window into past convergent events or ongoing mantle flow. The relationship between anisotropy and strain will be elaborated upon below. Notable tectonic settings where anisotropy is used to explain past or ongoing deformation include continental collision zones, subduction zones, and ocean basins [e.g. *Long and Silver,* 2009; *Silver,* 1996; *Wirth and Long,* 2012].

Anisotropy in the upper mantle forms when olivine and orthopyroxene grains align preferentially. This phenomenon, called lattice or crystalline preferred orientation (LPO or CPO) occurs when the dislocation creep deformation mechanism is active. While the pressure-temperature-stress conditions over which deformation creep is the dominant mechanism are still being mapped out, it is generally thought that most mantle anisotropy occurs in roughly the upper 200 km [*Karato et al.*, 2008; *Yuan and Romanowicz*, 2010]. Olivine is the primary cause of anisotropy in this region, and the effects of orthopoyroxene will be considered inconsequential [*Long and Becker*, 2010].

In most conditions olivine's crystallographic a-axis will align parallel to the mantle flow direction, while the b-axis orientates perpendicular to the flow direction [*Karato et al.*, 2008]. Shear wave velocity is fastest for energy travelling along the a-axis; therefore, it is deemed to be the fast axis while the b-axis is the slow axis [*Nicolas and Christensen*, 1987].

1.2.2 Shear Wave Splitting

As a shear wave encounters an anisotropic volume, it will split into two orthogonally polarized but separately propagating waves known as the fast and slow waves (Figure 1.2). [e.g. *Silver*, 1996]. This act of splitting waves is known as shear wave splitting (SWS). However, it is difficult to distinguish where along the ray path of an S-wave SWS occurs. Anisotropy may cause SWS near the source-side of the ray path, the receiver side, or both sides.

However, a particularly useful set of seismic ray paths--termed phases--are those that bottom out in the outer core, and then convert to an S-wave as they reenter the mantle. Since only P-waves can propagate through the liquid outer core and these are polarized along their ray path, when they pass the core-mantle boundary (CMB) and convert to a shear wave, the only shear wave motion that is excited is perpendicular to the ray path and in the direction that lies in the plane between the source and the receiver.

SKS and SKKS (Figure 1.3) are both examples of such phases that bottom out in the core. An SKS wave leaves the earthquake as an S-wave and coverts into a P-wave as it travels through the liquid outer core. It then converts back into an S-wave as it exits the CMB. An SKKS wave travels a similar path. It starts out as an S-wave, converts into a P-wave as it enters the CMB, then, unlike an SKS wave, it will bounce off the CMB back into outer core as a P-wave before it exists the CMB as an S-wave.

Because the SKS and SKKS phases have known polarizations when they leave the outer core, any deviation from this polarization direction indicates the wave-encountered anisotropy somewhere along the upward directed leg of the ray path. When seismic waves are recorded at a seismometer, the velocity of ground motion is recorded along two horizontal channels: N-S and E-W, and in the vertical direction. When measuring shear wave splitting, it is useful to rotate the horizontal channels such that one axis is in the direction between the seismometer and the earthquake--the radial direction--and one axis points perpendicular to this direction--the transverse or tangential direction. Because the tangential direction is perpendicular to the original polarization of the upcoming SKS or SKKS wave as it leaves the core, any motion in this direction is likely an indication of seismic anisotropy. If there is no transverse energy, then the wave encountered one of three scenarios. 1) The wave did not travel through an anisotropic medium. 2) The polarization of the wave is aligned with the fast axis. 3) The polarization of the wave is aligned with the slow axis. The latter two cases are known as null splits.

Shear wave splitting methods endeavor to estimate the azimuth of the fast axis polarization, commonly known as ϕ, and the delay time, δt, between the two components [*Silver*, 1996]. Together these measurements are known as the splitting parameters. The polarization direction generally tends to align with the maximum direction of strain, which in turn is sub-parallel to the mantle flow direction; however, other factors such as water content, pressure, and partial melting can alter its direction [*Karato et al.*, 2008]. The delay time depends on the path length through the anisotropic material and the perturbation in shear velocity, which is a function of the degree of alignment of the olivine grains [*Silver and Chan*, 1991].

1.2.3 Olivine Fabrics

Under differing temperature, stress, and water content conditions, olivine will deform in differing ways, producing a variety of types of alignment termed A-, B-, C-, D-, and E-type [*Karato et al.*, 2008]. A-type olivine favors low water content and modest stress and temperature conditions and is the more dominant fabric in the lithosphere [*Karato et al.*, 2008]. This study, therefore, will take as an opening hypothesis that the lithosphere beneath Japan contains A-type olivine. High water content can cause olivine to transition to a B-type fabric [*Karato et al.*, 2008]. B-type olivine is unlike the other fabrics because its fast axis aligns perpendicular to the mantle flow direction (Figure 1.4). It is theorized that trench-parallel ϕ found in some subduction zones could be due to the presence of B-type olivine [*Karato et al.*, 2008].

1.2.4 One Layer vs. Two Layer Modeling

Depending on the angle between the ray path of the wave and the fast axes polarizations of the medium, the amount of transverse energy produced will vary. The angle that the ray path enters the medium is known as the back azimuth of the ray. The back azimuth is the angle from north that the seismic wave travels relative to the recording station. Figure 1.5.a depicts synthetic impulse responses to a simple single layer of anisotropy that has a ϕ of 0°, for input radial impulses that have back azimuths varying from 0° to 180°. If the back azimuth is aligned with the fast axis (0° or 180°) or with the slow axis (90°), no splitting will occur and therefore no transverse energy will be detected. The greatest amount of transverse energy occurs when the initial polarization of the seismic wave is at a 45° angle from the fast axis, whereas the null splits, which occur when the back azimuth of the impulse occurs along the fast or slow axis orientations, have no transverse energy.

If, at a station, SKS or SKKS rays from a variety of back azimuths have no transverse energy, then one can conclude that either no anisotropy exists, the fast axes are vertically aligned, or anisotropy varies over scale lengths much smaller than the wavelengths of the SKS and SKKS [*Menke and Levin*, 2003].

When a ray passes through more than one layer of anisotropy, the impulse responses are more complex (Figure 1.5.b). The wave will split in response to the first layer of anisotropy it encounters, and then splits again as it travels through the second layer. The seismogram recorded detects the combination splitting due to these two layers. Figure 1.5.b depicts the impulse response if a wave first encounters a layer similar to Figure 1.5.a and then a second layer with a ϕ of 30°. The combination of the two layers produce complicated responses that are harder to analyze. Notably, the actual seismogram that is observed is the convolution of the SKS or SKKS waveform that is entering the anisotropic volume with the impulse response. Since these phases have wave periods on the order of 10 s, many of the details in the impulse will be invisible in the observed seismograms.

1.3 Motivation and Methodology

1.3.1 Motivation

Mantle flow patterns can provide the key to understanding the transportation of melts and volatiles, tectonic processes, and slab motion. Previous studies of the Japan subduction system using SWS of ScS waves (an S-wave that bounces off the outer core) [*Hiramatsu et al.*, 1997] and direct S-waves *[Long and van der Hilst*, 2006; *Wirth and Long*, 2010], P-wave tomography [*Wang and Zhao*, 2008], and P to S receiver function analysis [*Nagaya et al*., 2011; *Wirth and Long*, 2012] have found that trench-parallel fast axes tend to be found closer to the trench whereas trench-perpendicular fast axes are found further away from the trench (Figure 1.6). These differing fast axes raise the question of how the mantle wedge flow in Japan's subduction system.

If only A-type olivine were present in the subduction system, the differing fast axes orientations would imply that the mantle is flowing parallel to the trench closer to it and is flowing perpendicular to the trench further away. However, if B-type olivine were present in the mantle wedge near the trench, the fast axes in this part of the system would align perpendicular to the mantle flow direction while the fast axes of the A-type olivine located further from the trench would align parallel to mantle flow. This would imply that the mantle wedge is flowing perpendicular to the trench throughout the system.

The goal of this study is to better constrain the complex mantle anisotropy beneath Japan to enhance the current understanding of mantle wedge flow in subduction systems. This study measures splitting parameters of SKS and SKKS waves using adaptations of the method proposed by *Silver and Chan* [1991] as described in the following section.

1.3.2 Silver and Chan

As SWS has grown in popularity as a tool for measuring seismic anisotropy, several different analysis methods have been developed. *Long and Silver* [2009] have summarized several of these techniques including the transverse component minimization method developed by *Silver and Chan* [1991]. The goal of this method is to try to find the original SKS (or SKKS) wave prior to splitting, which has no particle motion in the transverse direction [*Silver and Chan*, 1991].

Using a grid search approach, all possible combinations of δt and ϕ values from 0-4 seconds and -180°-+180°, respectively, are tested [*Long and Silver*, 2009]. For a given splitting set of splitting parameters, the observed radial and transverse seismograms are rotated to the assumed fast-slow axis orientation. Then the presumed fast and slow waves are delayed and advanced, respectively, by the assumed $\delta t/2$. For example, for a posited splitting parameter pair of $\phi = 100°$ and $\delta t = 2$ s, the observed radial seismogram is rotated to 100° and the observed transverse seismogram to 10°. If the rotation is correct, the fast-polarized wave will appear on the previous radial channel, and the slow polarized wave will appear on the previous transverse channel. Then, the presumed fast and slow waves are delayed and advanced, respectively, by 1 second. The resulting waves are rotated back into the radial-transverse reference frame as "corrected radial" and "corrected transverse." The amount of energy that remains on the "corrected transverse" is then measured and plotted on a δt versus ϕ contour plot [*Long and Silver*, 2009]. For the optimal values of ϕ and δt, the corrected transverse energy will be minimized.

This method does, however, make a few assumptions. First it assumes that only one layer of anisotropy is present. This implies that if more than one layer of anisotropy is present, than the stronger anisotropic medium is controlling the splitting parameters. Secondly, this method assumes the alignment of fast axes of olivine is uniform throughout the anisotropic medium. Lastly, this method assumes that the anisotropic layer is not dipping.

1.4 Figures

a) b)

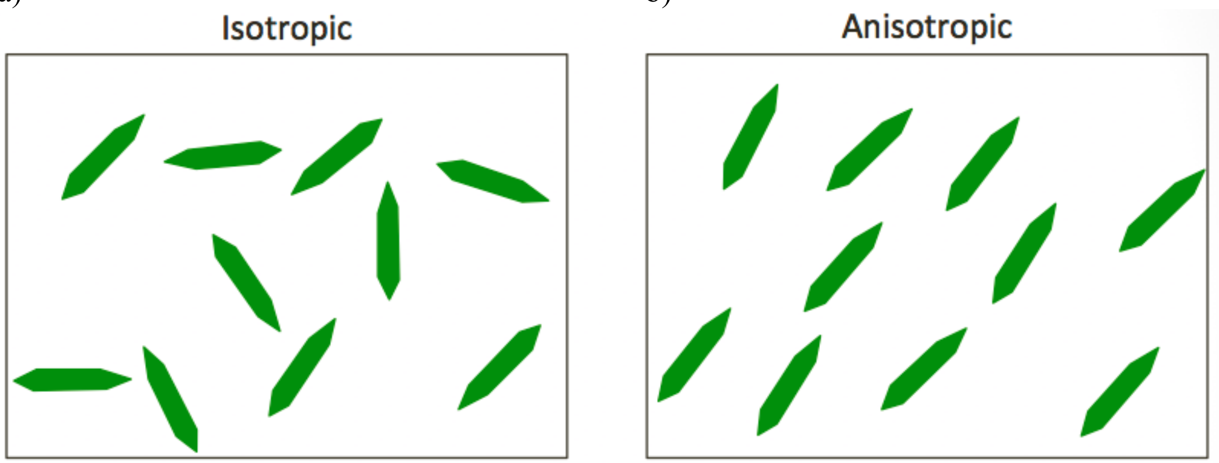

Figure 1.1: A cartoon drawing of olivine crystals in an (a) isotopic medium and an (b) anisotropic medium.

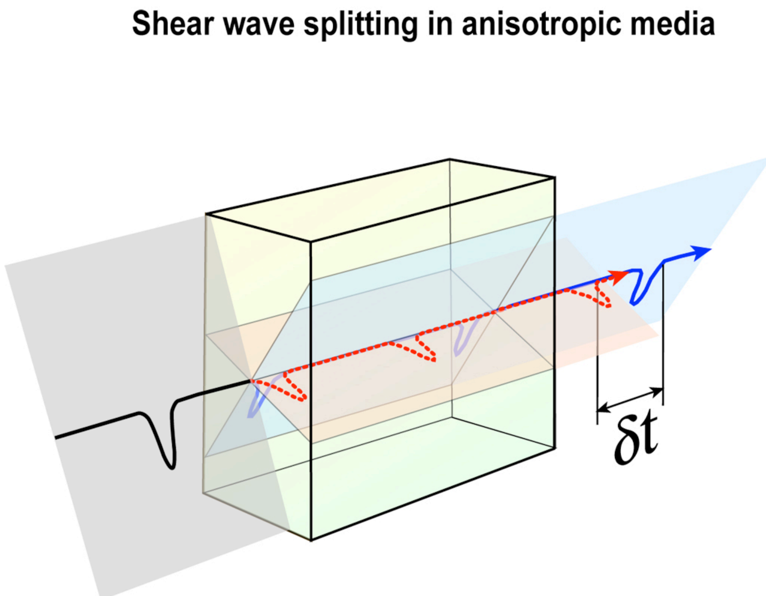

Figure 1.2: A cartoon of shear wave splitting in an anisotropic media. The shear wave (black line) originally travels in the radial plane (grey plane). As it enters an anisotropic medium (yellow box), it splits into two polarized propagating waves. The blue line in this figure is traveling along the fast axis and exits the medium first. The red line is orthogonal to the blue and travels at a slower speed through the anisotropic medium. The delay time, δt, between the two arrivals is indicated. This image is from Ed Garnero [Unpublished, 2012] (http://garnero.asu.edu/research_images/images_anisotropy.html).

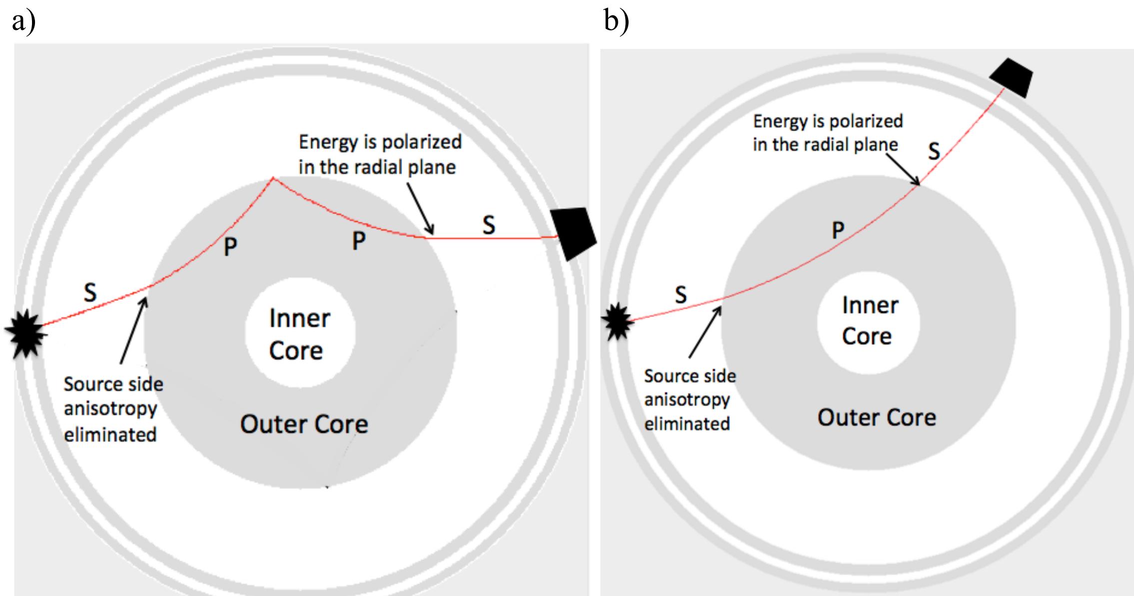

Figure 1.3: A sketch drawing of a cross section through the Earth. The starburst represents the earthquake, and the polygon is the receiver. a) The red line is the path of an SKS wave. As the wave is emitted from the hypocenter, it starts as an S-wave. When the wave hits the outer core it transforms its energy into a P-wave. After leaving the outer core, the wave turns back into an S-wave with its shear energy polarized in the radial plane. b) The red line is the path of an SKKS wave. An SKKS wave has a similar path of an SKS wave, but it bounces back into the outer core once before it reenters the mantle.

a)

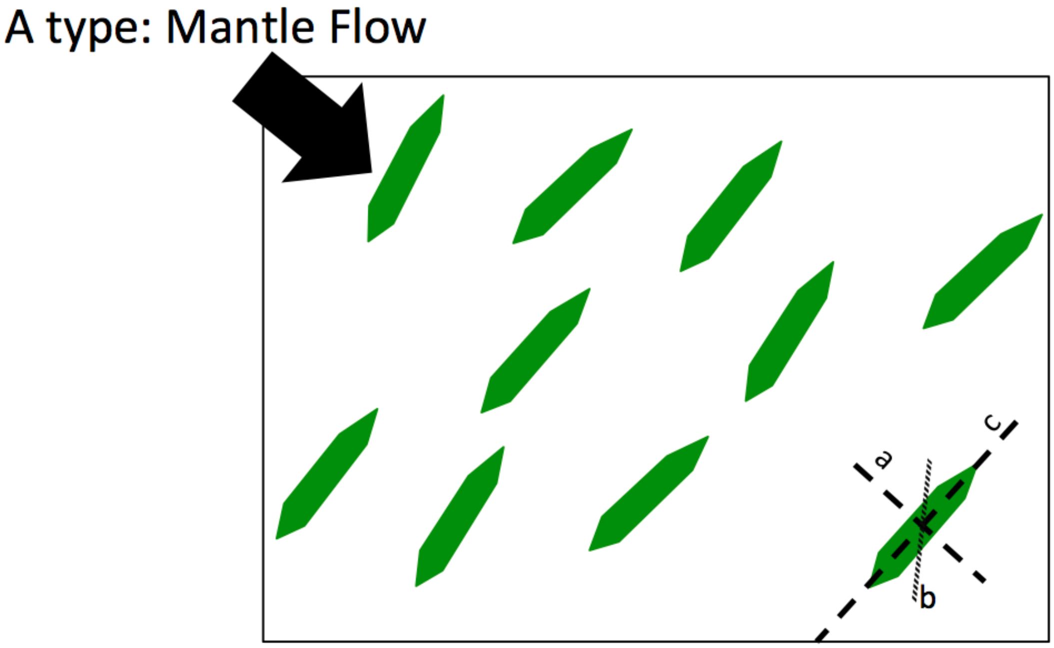

b)

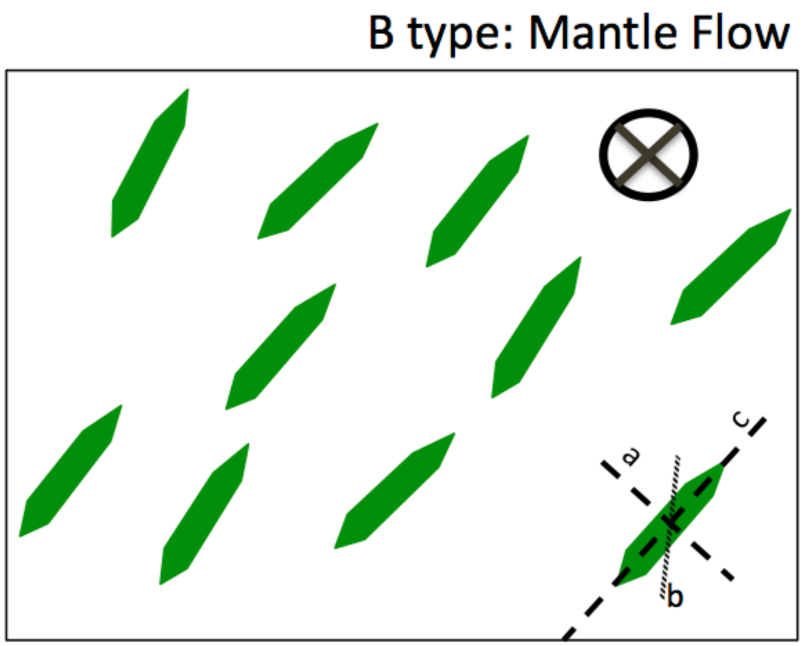

Figure 1.4: Cartoon sketches of mantle flow directions for A-type and B-type olivine. The bottom right olivine crystal in each sketch shows the alignment of olivine axes. The a-axes are aligned in a plane from the top left corner to the bottom right corner. The b-axes are going into the page. The c-axes are aligned in a plane from the bottom left corner to the top right corner. a) Fast axes directions for A-type olivine align such that they are parallel to mantle flow direction; therefore, in this sketch mantle flow is towards the bottom right corner. b) Fast axes directions for B-type olivine align such that they are perpendicular to mantle flow direction; therefore, in this sketch mantle flow is into the page. The greatest amount of transverse energy occurs when the initial polarization of the seismic wave is at a 45° angle from the fast axis.

a)

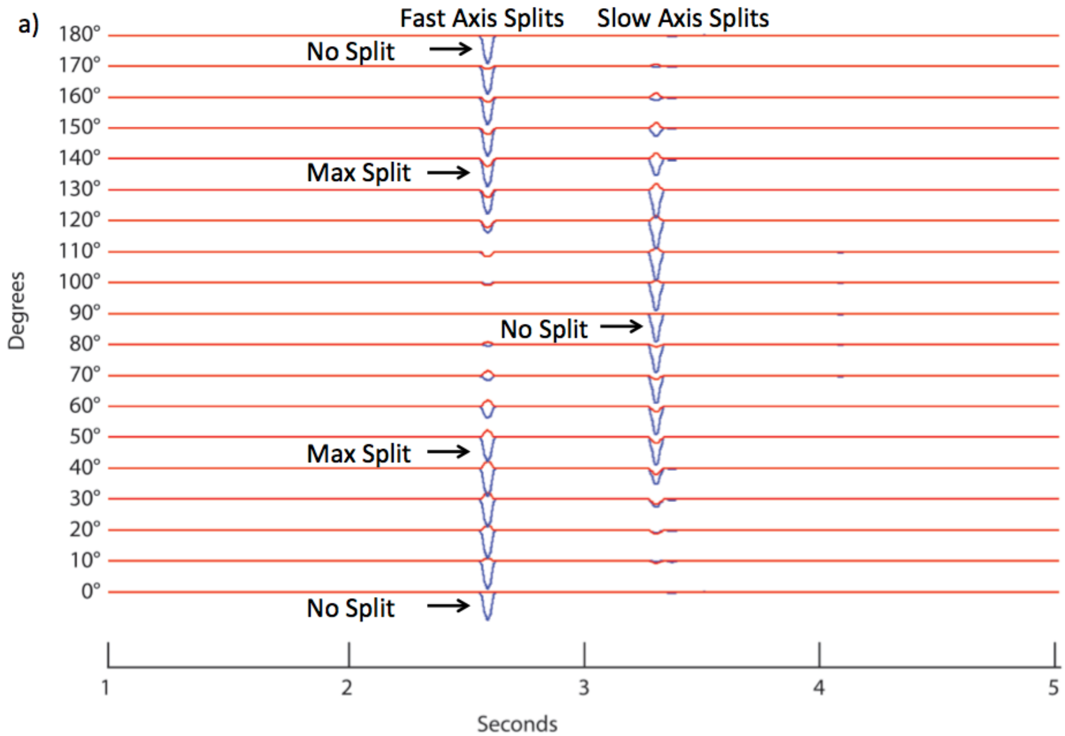
Fast Axis Splits
Slow Axis Splits
No Split
Max Split
No Split
Max Split
No Split
180°
170°
160°
150°
140°
130°
120°
110°
100°
90°
80°
70°
60°
50°
40°
30°
20°
10°
0°
Degrees
1
2
3
4
5
Seconds

b)

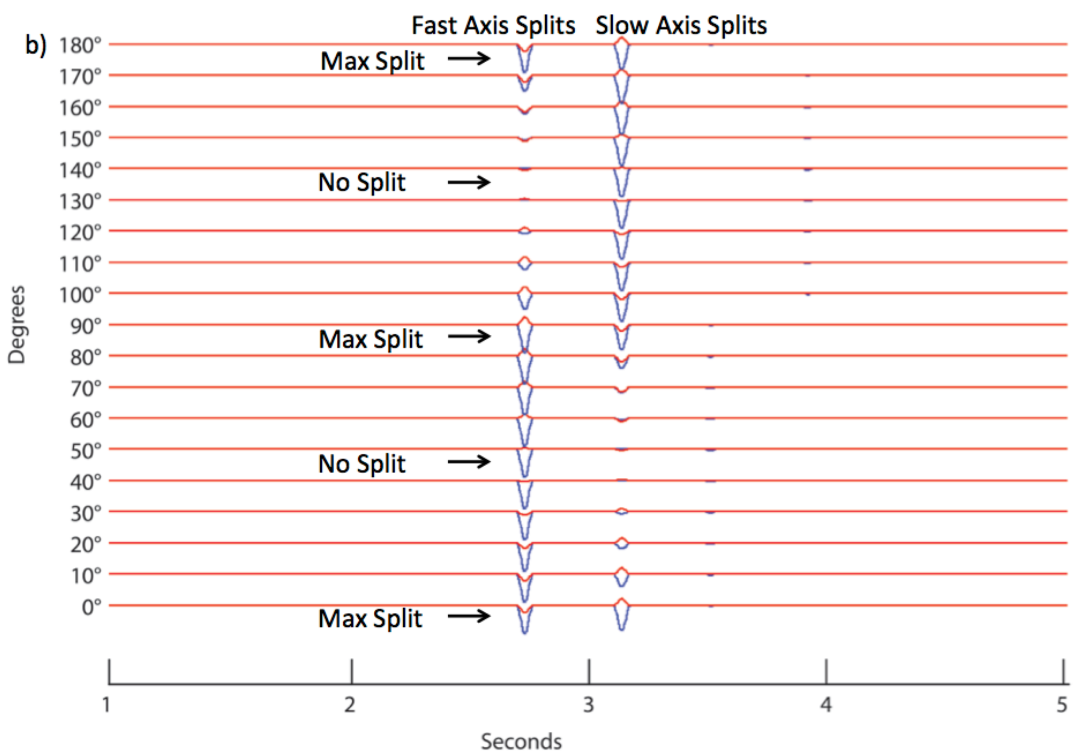
Fast Axis Splits
Slow Axis Splits
Max Split
No Split
Max Split
No Split
Max Split
180°
170°
160°
150°
140°
130°
120°
110°
100°
90°
80°
70°
60°
50°
40°
30°
20°
10°
0°
Degrees
1
2
3
4
5
Seconds

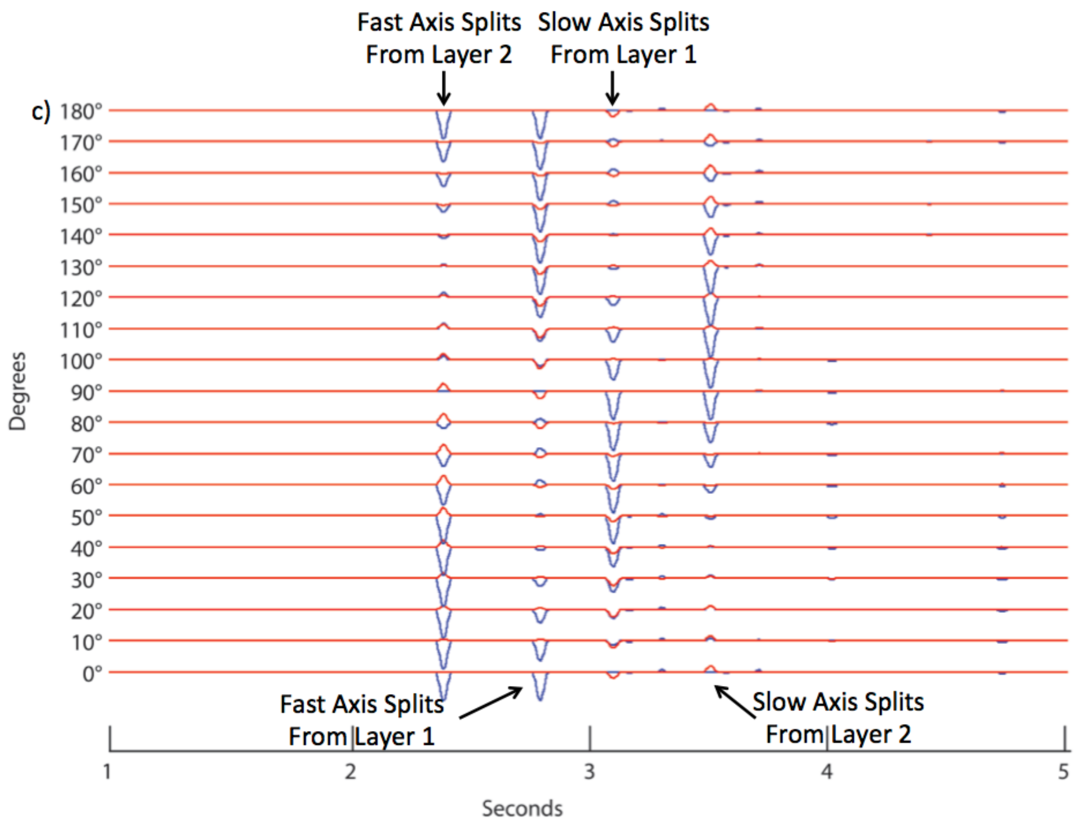

Figure 1.5: Synthetic impulse responses over varying back azimuths. The blue line is the radial component and the red line is the transverse component. a) These impulse responses are from a wavelet that traveled through a single anisotropic layer with the fast axis polarization of 0°. When the wavelet enters the anisotropic medium aligned with the fast axis, 0° or 180°, or with the slow axis, 90°, no splitting occurs and no transverse energy is produced. The greatest amount of transverse energy is created when the wavelet enters the medium at a 45° angle. b) These impulse responses are from a wavelet that traveled through a single anisotropic layer with the fast axis polarization of 45°. When the wavelet enters the anisotropic medium aligned with the fast axis, 45°, or with the slow axis, 135°, no splitting occurs therefore no transverse energy is produced. The greatest amount of transverse energy is created when the wavelet enters the medium at a 45° angle from the fast or slow axes, 0°, 90° or 180°. c) These impulse responses are from a wave that traveled through two anisotropic layers. The first layer had the same parameters as a) and the second layer had the same parameters as b). The overall impulse response becomes more complicated and harder to analyze when the wave has traveled through multiple layers.

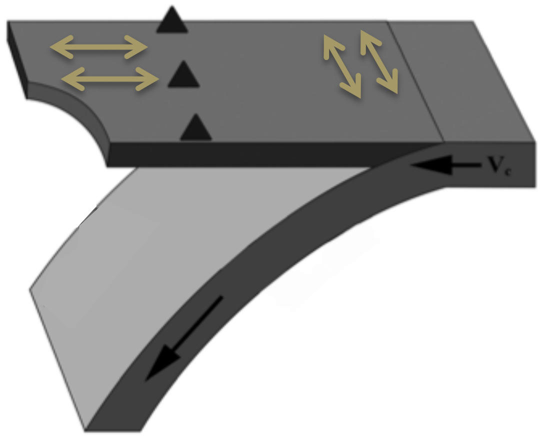

Figure 1.6: A cartoon sketch of fast axes polarizations after *Long and Wirth* [2013]. The gold arrows represent fast axes directions. Previous studies have found trench-parallel fast axes closer to the trench, and trench-perpendicular fast axes further away from the trench.

REFERENCES

Alsina, D., and R. Snieder (1995), Small-Scale Sublithospheric Continental Mantle Deformation - Constraints from Sks Splitting Observations, *Geophys J Int*, *123*(2), 431-448, doi:Doi 10.1111/J.1365-246x.1995.Tb06864.X.

Crotwell, H. P., T. J. Owens, and J. Ritsema (1999), The TauP Toolkit: Flexible Seismic Travel-time and Ray-path Utilities, *Seismological Research Letters*, *70*(2), 154-160, doi:10.1785/gssrl.70.2.154.

Hiramatsu, Y., M. Ando, and Y. Ishikawa (1997), ScS wave splitting of deep earthquakes around Japan, *Geophys J Int*, *128*(2), 409-424, doi:Doi 10.1111/J.1365-246x.1997.Tb01564.X.

Karato, S., H. Jung, I. Katayama, and P. Skemer (2008), Geodynamic significance of seismic anisotropy of the upper mantle: New insights from laboratory studies, *Annu Rev Earth Pl Sc*, *36*, 59-95, doi:Doi 10.1146/Annurev.Earth.36.031207.124120.

Long, M. D., and T. W. Becker (2010), Mantle dynamics and seismic anisotropy, *Earth Planet Sc Lett*, *297*(3-4), 341-354, doi:Doi 10.1016/J.Epsl.2010.06.036.

Long, M. D., and P. G. Silver (2009), Shear Wave Splitting and Mantle Anisotropy: Measurements, Interpretations, and New Directions, *Surv Geophys*, *30*(4-5), 407-461, doi:Doi 10.1007/S10712-009-9075-1.

Long, M. D., and R. D. van der Hilst (2006), Shear wave splitting from local events beneath the Ryukyu arc: Trench-parallel anisotropy in the mantle wedge, *Phys Earth Planet In*, *155*(3-4), 300-312, doi:Doi 10.1016/J.Pepi.2006.01.003.

Long, M. D., and E. A. Wirth (2013), Mantle flow in subduction systems: The mantle wedge flow field and implications for wedge processes, *J Geophys Res-Sol Ea*, *118*(2), 583-606, doi:Doi 10.1002/Jgrb.50063.

Menke, W., and V. Levin (2003), The cross-convolution method for interpreting SKS splitting observations, with application to one and two-layer anisotropic earth models, *Geophys J Int*, *154*(2), 379-392, doi:Doi 10.1046/J.1365-246x.2003.01937.X.

Nagaya, M., H. Oda, and T. Kamimoto (2011), Regional variation in shear-wave polarization anisotropy of the crust in southwest Japan as estimated by splitting analysis of Ps-converted waves on receiver functions, *Phys Earth Planet In*, *187*(1-2), 56-65, doi:Doi 10.1016/J.Pepi.2011.04.016.

Nicolas, A., and N. I. Christensen (1987), Formation of Anisotropy in Upper Mantle Peridotites - A Review, in *Composition, Structure and Dynamics of the Lithosphere-Asthenosphere System*, edited, pp. 111-123, American Geophysical Union, doi:10.1029/GD016p0111.

Silver, P. G. (1996), Seismic anisotropy beneath the continents: Probing the depths of geology, *Annu Rev Earth Pl Sc*, *24*, 385-432, doi:Doi 10.1146/Annurev.Earth.24.1.385.

Silver, P. G., and W. W. Chan (1991), Shear-Wave Splitting and Subcontinental Mantle Deformation, *J Geophys Res-Sol Ea*, *96*(B10), 16429-16454, doi:Doi 10.1029/91jb00899.

Wang, J., and D. P. Zhao (2008), P-wave anisotropic tomography beneath Northeast Japan, *Phys Earth Planet In*, *170*(1-2), 115-133, doi:Doi 10.1016/J.Pepi.2008.07.042.

Wirth, E., and M. D. Long (2010), Frequency-dependent shear wave splitting beneath the Japan and Izu-Bonin subduction zones, *Phys Earth Planet In*, *181*(3-4), 141-154, doi:Doi 10.1016/J.Pepi.2010.05.006.

Wirth, E. A., and M. D. Long (2012), Multiple layers of seismic anisotropy and a low-velocity region in the mantle wedge beneath Japan: Evidence from teleseismic receiver functions, *Geochem Geophy Geosy*, *13*, doi:Artn Q08005: Doi 10.1029/2012gc004180.

Yuan, H. Y., and B. Romanowicz (2010), Depth dependent azimuthal anisotropy in the western US upper mantle, *Earth Planet Sc Lett*, *300*(3-4), 385-394, doi:Doi 10.1016/J.Epsl.2010.10.020.

CHAPTER 2

MEASURING SEISMIC ANISOTROPY IN THE MANTLE WEDGE OF JAPAN'S SUBDUCTION SYSTEM USING SHEAR WAVE SPLITTING OF SKS AND SKKS WAVES

2.1 Introduction

2.1.1 Mantle Anisotropy and Shear Wave Splitting

Seismic anisotropy can provide information about the flow of the asthenosphere and past deformation of the lithosphere. Olivine grains in the upper mantle show a preferential alignment of crystallographic orientations with strain, or lattice preferred orientation (LPO) [e.g. *Karato et al.*, 2008; *Menke and Levin*, 2003; *Silver and Chan*, 1991]. As a seismic wave travels through an anisotropic region, shear wave splitting (SWS), a process similar to birefringence, will occur. The incident wave will split into two orthogonally polarized but separately propagating waves [*Silver*, 1996]. The fastest wave will travel along an axis known as the "fast axis", typically aligned with the a-axis of olivine. The slower traveling wave will be polarized along the "slow axis."

Shear wave splitting techniques aim to measure the fast axis polarization direction, ϕ, and the delay time, δt, between two the two components [*Silver*, 1996]. Together these measurements are known as the splitting parameters. The polarization direction can approximately be considered to be parallel to the mantle flow direction, but other factors such as water content, pressure, and partial melting can alter its direction [*Karato et al.*, 2008]. The delay time depends on the path length through the anisotropic material and the perturbation in shear velocity [*Silver and Chan*, 1991], which is a function of the strain history of the material.

Anisotropy is commonly measured through SWS of SKS and SKKS waves. The advantage of using SKS and SKKS waves is that as the P-wave converts into an S-wave in the outer core it becomes radially polarized, eliminating any prior effect of anisotropy along the source-side path (Figure 2.1) [*Silver*, 1996]. This means that if there is any amount of transverse energy component detected, the wave traveled through an anisotropic medium after it left the core mantle boundary (CMB). If there is no transverse energy, then either no anisotropy was encountered, or the polarization of the wave aligned with the fast or slow axes of the anisotropic material.

2.1.2 Motivation

Mantle flow patterns can provide the key to understanding the transportation of melts and volatiles, tectonic processes, and slab motion. Previous studies of the Japan subduction system using SWS of ScS waves (an S-wave that bounces off the outer core) [*Hiramatsu et al.*, 1997] and direct S-waves *[Long and van der Hilst*, 2006; *Wirth and Long*, 2010], P-wave tomography [*Wang and Zhao*, 2008], and P to S receiver function analysis [*Nagaya et al*., 2011; *Wirth and Long*, 2012] have found that trench-parallel fast axes tend to be found closer to the trench whereas trench-perpendicular fast axes are found further away from the trench. These differing fast axes raise the question of how the mantle wedge flow in Japan's subduction system.

If only A-type olivine were present in the subduction system, the differing fast axes orientations would imply that the mantle is flowing parallel to the trench closer to it and is flowing perpendicular to the trench further away. However, if B-type olivine were present in the mantle wedge near the trench, the fast axes in this part of the system would align perpendicular to the mantle flow direction while the fast axes of the A-type olivine located further from the trench would align parallel to mantle flow. This would imply that the mantle wedge is flowing perpendicular to the trench throughout the system.

The goal of this study is to better constrain the complex mantle anisotropy beneath Japan to enhance the current understanding of mantle wedge flow in subduction systems. This study measures splitting parameters of SKS and SKKS waves using adaptations of the method proposed by *Silver and Chan* [1991] as described in Section 2.5.

2.2 Tectonic Setting

Presently, the Japanese Islands sit on two tectonic plates, while two other plates subduct underneath the islands (Figure 2.2) [*Mahony et al.*, 2011]. From central Japan to the north, the islands sit on the North American plate which is underlain by the subducting Pacific plate. The islands south of central Japan sit on the Eurasian Plate under which the Philippine Sea plate is subducting. The Sea of Japan opened as a large back arc basin during the late Cretaceous [*Mahony et al.*, 2011]; extension ceased in the mid-Miocene [*Tatsumi and Kimura*, 1991]. A recent study by *Choi et al.* [2012] has found evidence for compressional stress fields in the rifted margins of the Sea of Japan. This may suggest the subduction zone is advancing westward and the Sea of Japan is closing [*Choi et al.*, 2012].

The trenches associated with subduction near Japan are, from south to north, called the Ryukyu Trench, Nankai Trough, Japan Trench, and Kuril Trench. Both the Ryukyu Trench and Nankai Trough are created by subduction of the Philippine Sea plate under southern Japan. The western part of the Philippine Sea plate formed from 40-60 Ma and is being subducted normal to the Ryukyu Trench at a rate of 79 mm/yr [*Mahony et al.*, 2011]. The eastern part of the Philippine Sea plate formed between 15-26 Ma and is being subducted approximately normal to the Nankai Trough at 72 mm/yr [*Mahony et al.*, 2011]. At the Japan and Kuril Trenches, 130 m.y. old Pacific plate is being subducted at a rate of 90 mm/yr [*Mahony et al.*, 2011]. The Pacific plate motion at the Japan Trench is approximately perpendicular to the trench, while its motion at the Kuril Trench is about 30° west of the trench [*Mahony et al.*, 2011].

For results and discussion purposes, the Japanese Islands have been separated into four study areas based on plate motions, subduction rates and trench locations. The dotted brown lines in Figure 2.2 represent the boundaries between the different subdivisions. This study refers to each area by the trench located in the section; Ryukyu Trench, Nankai Trough, Japan Trench, Kuril Trench.

Large-scale volcanism has occurred throughout the Japanese islands since the late Cretaceous [*Uyeda and Miyashiro*, 1974]. Compared to the rest of Japan, the Nankai Trough section has very few volcanoes. This lack of volcanism can be contributed to the shallow subduction angle of the eastern part of the Philippine Sea plate [*Mahony et al.*, 2011]. Even though the plate is young and hot, the shallow subduction angle prevents volatiles from being released by the plate closer to the trench; therefore, there are a limited number of volcanoes along the Nankai Trough [*Mahony et al.*, 2011].

2.3 Mantle Wedge Flow Models

Long and Wirth [2013] describe several mantle wedge flow models to describe the varying types of fast axes polarizations found in subduction systems. Figure 2.3.a depicts the simplest model. This model is characterized by 2-D corner flow caused by downdip motion of the slab [*Long and Wirth*, 2013]. As the slab is being subducted, it induces downward flow of the mantle wedge. The mantle near the surface then fills in the wedge near the trench. This model assumes A-type olivine deformation in which strain has aligned the fast axes with mantle flow to produce trench-perpendicular ϕ [*Long and Wirth*, 2013].

Previous studies of subduction zone anisotropy have found that many systems have trench-parallel ϕ in the mantle wedge as well as trench-perpendicular ϕ [*Collings et al.*, 2013; *Conder and Wiens*, 2007; *Maruyama et al.*, 1997; *Wirth and Long*, 2012]. This leads to the slightly more complex B-type Olivine Corner Flow Model (Figure 2.3.b). The overall mantle wedge flow in this model is the same as in the 2D corner flow model described above. High water content in the downgoing slab could have B-type olivine deformation, which during strain orients the fast axis perpendicular to flow causing a trench-parallel ϕ [*Karato et al.*, 2008]. In addition to water, high pressures and low temperatures would be needed to produce high enough stress and to activate the B-type olivine slip systems [*Karato et al.*, 2008]. If B-type olivine were present, it would likely be restrained to a small thin layer above the slab. This would leave to trench-parallel ϕ near the trench where B-type olivine would be found, and trench-perpendicular ϕ further away from the trench where A-type olivine would occur [*Long and Wirth*, 2013].

The model in Figure 2.3.c assumes A-type olivine deformation and depicts the Trench-parallel Mantle Flow Model. Internal pressure gradients due to trench migration coupled with a low viscosity channel could cause parallel mantle flow within a subduction system without presence of B-type olivine [*Conder and Wiens*, 2007]. Trench migration would push subslab mantle around the edge of the slab causing it to flow parallel to the trench [*Long and Silver*, 2008]. This model assumes decoupling of the downgoing slab from the wedge and predicts a correlation between δt and trench migration rate [*Long and Wirth*, 2013]. This model would explain the occurrence of trench-parallel ϕ, but is unable to produce a trench-perpendicular ϕ further away from the trench.

Long and Silver [2008] adapted this model to account for trench-perpendicular ϕ and trench-parallel ϕ (Figure 2.3.d). Their model combines trench migration induced flow and down dip induced corner flow [*Long and Silver*, 2008]. Trench migration causes subslab mantle to flow parallel to the trench as in the Trench-parallel model while corner flow down dip creates trench-perpendicular ϕ. Large delay times would predict that the subduction system is undergoing trench migration [*Long and Wirth*, 2013].

2.4 Data

Seismograms used in this survey were collected through the Japanese National Research Institute for Earth Science and Disaster Preventions (NIED) F-net Broadband Seismograph Network (**http://www.fnet.bosai.go.jp**). Seismograms between January 1st, 2000 and December 31st, 2013 were requested for events with a 6.5 magnitude earthquake or larger. Events for each of F-net's 84 stations needed to be located within a radial distance of 85° to 125° and 95° to 180° to produce SKS and SKKS waves, respectively. With these criteria 114 possible SKS events and 133 possible SKKS events were downloaded. Events were then rotated to radial and transverse components.

Event information including location, magnitude and depth was obtained through the Standing Order for Data (SOD) program [*Owens et al.*, 2004]. With the event information predicted SKS and SKKS arrival times were calculated using *Dziewonski and Anderson's* [1981] Preliminary Reference Earth Model (PREM). Any seismogram that had another predicted phase arrival within 20 seconds of the predicted SKS and SKKS arrival times was removed from the data set. This was done to prevent any overlapping phase energy from skewing the splitting results.

A visual inspection was done to manually adjust SKS/SKKS arrival times to fit the data and to remove any event without an apparent SKS/SKKS arrival (Figure 2.4). The signal window used for analysis was defined as starting from the first visually apparent onset of the SKS/SKKS, to 15 seconds thereafter. The portion of the seismogram prior to the defined onset was considered to be noise, while anything after the signal window was ignored. Any seismogram that had a signal-to-noise ratio (SNR) less than 2.5 was also removed from the data set as it was considered to be too noisy.

2.5 Method

To estimate splitting parameters, this study uses the *Silver and Chan* [1991] approach, in which a grid search is run over all reasonable combinations of δt and ϕ (values from 0-4 seconds and 0-180°, respectively). This method seeks the δt, ϕ pair that best corrects for anisotropy, measured by how well the transverse energy is minimized. Two minor modifications were made to the *Silver and Chan* [1991] method. The first is that pre-SKS noise is measured and used as a "water-level" under which the corrected tangential energy is not allowed to go. This removes the possibility that seismic noise may modify the observed signal in such a way that produces a spurious minimum in the corrected transverse energy when the grid search is run, which in turn reduces the possibility of having overly small confidence bounds on estimates of the splitting parameters. A second minor modification from *Silver and Chan* [1991] is that corrected transverse energy, as a function of splitting parameters, is mapped into a probability density function that is a function of the splitting parameters, following the same approach as *Silver and Chan* [1991] does to identify the 67% confidence interval (Figure 2.5).

We are aware that mantle flow in a subduction zone may be such that two or more layers of anisotropy, or other complexity in anisotropy, could be occurring. This complexity would produce splitting parameters that vary with the back azimuth of the event [*Silver and Savage*, 1994]. However, the data is insufficient to constrain anisotropic complexities, and the simplest reasonable anisotropic structures will be assumed.

2.6 Further Data Processing

Before plotting the resulting splitting parameters from *Silver and Chan's* [1991] method a few more seismograms were removed. Calculated splitting parameters that had an unrealistic 67% Gaussian confidence interval were deemed unreliable and removed from the data set. Seismograms that produced delay times greater than 3 seconds were removed as well. Delay times are typically at most 1 or 2 seconds. Any delay time greater than this is thought to be unrealistic based on the current understanding of anisotropic media in the mantle [*Plomerova et al.*, 1998; *Wustefeld et al.*, 2008]. This left 27 events (or individual earthquakes), 60 stations, and 153 radial and transverse seismogram pairs, which were deemed to be "Good Events." From the "Good Events" any seismogram with a δt error greater than 0.8 seconds and a ϕ error greater than 60° was deemed too noisy and removed from the data set. A second visual inspection was done to remove any weaker SKS/SKKS signals. The remaining signals were divided into two groups, "Better Events" and "Best Events."

A seismogram that would be considered a "Good Event" needed to have an apparent SKS/SKKS signal in the radial plane. Seismograms that were included in this category included events similar to Figure 2.6.a. This first visual inspection was looking for anything that had energy on the radial plane near the predicted arrival time. All "Better Events" and "Best Events" are included in this category.

Seismograms with really long periods were not included in "Better Events". Seismograms with high frequency noise were also not included in "Better Events." These events were excluded because it is thought that the error calculation in *Silver and Chan* [1991] underestimates error bars for noisier events. Visible energy on the tangential plane was needed for a seismogram to be considered a "Better Event." Figure 2.6.b shows a seismogram that would qualify as a "Better Event." All "Best Events" were included in "Better Events." "Better Events" included 24 stations, 13 events, and 35 radial and transverse seismogram pairs.

Only events with strong SKS/SKKS wave arrivals were included in "Best Events." This included events with typical SKS/SKKS periods, high SNR, and clear tangential energy. Figure 2.6.c shows an SKS seismogram that fits all the criteria for "Best Events." "Best Events" included 21 stations, 7 events, and 28 radial and transverse seismogram pairs.

A list of station information for stations used in this study can be found in Table 2.1. Table 2.2 contains a list of earthquakes used in this study including the number of radial and transverse seismogram pairs used for each event. Figure 2.7 plots the locations of the events used in each data group.

2.7 Results

Figure 2.8 maps the "Good Events" results (Table 2.3). Error bars were left off this figure, as there are so many events with varying amounts of error that the individual results could not be deciphered. There appears to be a north-south trend and an east-west trend of fast axes directions, but these are most likely null events as they both occur at many stations. Ignoring these null events, it is hard to identify any real pattern. It is due to this lack of pattern and the uncertainty of noisy splitting parameters that the data selections for "Better Events" and "Best Events" as described in Section 2.6 were made.

A map of "Better Events" results (Table 2.4) can be seen in Figure 2.9. Although the data is still complex, a pattern starts to become clearer. The Ryukyu trench section has trench-parallel fast axes trends closer to the trench especially on the southern islands. On the main island near the northern part of this section, the fast axes are aligned perpendicular to the trench. These trench-perpendicular trends are further away from the trench.

The Nankai Trough results for "Better Events" show that most fast axes directions are aligned parallel to plate motion, which is almost normal to the trench [*Mahony et al.*, 2011]. Stations close to the Japan Trench have trench-parallel fast axes. The stations further away from the trench, especially in the southern part of this section, have trench-perpendicular fast axes. Fast axes near the Kuril Trench do not show as clear of a pattern. Plate motion in this section is about 30° west from the trench. The fast axes directions at the southernmost and the easternmost stations of this section are approximately parallel to plate motion, while fast axes between those stations are nearly perpendicular to plate motion.

The "Best Events" results (Table 2.5) include the strongest SKS and SKKS wave arrivals and are plotted in Figure 2.10. The fast axes trends are more prominent than "Better Events" results. The Ryukyu Trench has trench-parallel fast axes closer to the trench and trench-perpendicular fast axes further away. The fast axes in the Nankai Trough are nearly aligned with plate motion. The Japan Trench has trench-parallel trends as well as trench-perpendicular trends. The events left near the Kuril Trench are roughly perpendicular to plate motion.

2.8 Discussion

2.8.1 The Ryukyu Trench and Japan Trench

The complexity of "Good Events" results suggests that the possibility cannot be excluded that more than one layer of anisotropy exists. Since insufficient data exist to readily characterize multi-layer anisotropy, it will be assumed that splitting parameters are indicative of a single "dominant layer" of anisotropy. The dominant layer refers to the layer with stronger anisotropic properties, typically the thicker layer. The shear wave traveling through this layer will undergo more splitting than the other layer(s). Therefore, it is the layer that will cause the greatest amount of delay time and thus control the fast axes orientations.

The results for “Better Events” and “Best Events” in both the Ryukyu Trench section and the Japan Trench section show trench-parallel fast axes near the trench and trench-perpendicular trends further away. This is consistent with either the B-type Olivine model or the *Long and Silver* [2008] model (Figure 2.3). If exclusively A-type olivine is assumed, stations with trench-perpendicular fast axes indicate that the mantle is flowing perpendicular to the trench under those stations and in the direction of plate subduction. Trench-parallel fast axes would then indicate flow perpendicular to the converge direction.

For subslab mantle to flow around the edges of the trench and parallel to the trench as this model implies, trench migration, advancing or retreating, is needed. Focal mechanisms from earthquakes found in the Sea of Japan indicate convergence, implying the trenches around Japan are migrating eastwards [*Choi et al.*, 2012]. However, no trench-parallel fast axes are observed near the Nankai Trough, suggesting either trench migration is not large enough to stimulate along-strike mantle flow, or that *Long and Silver’s* [2008] model does not explain the SWS around Japan.

The B-type Olivine Model can also explain the trench-parallel and trench-perpendicular trends seen in the Ryukyu Trench and Japan Trench sections. B-type olivine favors high stress, low temperature, and high water content conditions (Figure 2.11) [*Karato et al.*, 2008]. The Pacific plate subducting underneath the Japan Trench is about 130 m.y. old, and the western part of the Philippine Sea plate subducting underneath the Ryukyu trench is at least 40 m.y. old [*Mahony et al.*, 2011]. Both of these plates are old enough that temperatures would be cold enough to support the high stress conditions under which B-type olivine would occur. In a review of water content in the upper mantle, *Karato* [2003] states that water content in the mantle is likely localized beneath volcanoes. The numerous volcanoes in both the Ryukyu Trench and Japan Trench sections could therefore indicate high water content in the mantle wedge. *Karato* [2003] also suggests that the presence of lower than expected temperatures above the subducted Pacific plate beneath Japan implies a usually high amount of water content in olivine crystals.

A study done by *Nozaka* [2005] on the Happo ultramafic complex, a surface exposure in central Japan, found the LPO of olivine crystals in the complex to be that of B-type olivine [*Nagaya et al.*, 2014]. If B-type olivine is found at the surface, it is reasonable to assume that it can also be found in the mantle wedge. *Nagaya et al.* [2014] argue that antigorite-bearing mantle is thought to be widespread in the forearc of Japan's subduction zone. Since antigorite, a member of the serpentine group, has similar properties as B-type olivine, B-type olivine can grow on top of the subducting antigorite crystals [*Nagaya et al.*, 2014].

Figure 2.12 illustrates the possible location of B-type olivine in a subduction system using the Japan Trench as a model [*Nagaya et al.*, 2014]. This figure suggests that even though there is B-type olivine along most of the downgoing slab, further away from the trench there is a thicker layer of A-type olivine on top of the B-type olivine layer. The thicker layer of A-type olivine would therefore be the dominant layer and will control fast axis further away from the trench.

Presence of B-type olivine at the surface, the subduction of antigorite-bearing minerals, the unusually high water content, and the older plates are all evidence that B-type olivine could be present in the Japan Trench. Previous studies of anisotropy near the Ryukyu Trench have found trench-parallel fast axis patterns and have linked it to the presence of B-type olivine [*Kneller et al.*, 2008; *Nagaya et al.*, 2014]. The past studies, along with the age of western part of the Philippine Sea plate, and presence of volcanoes all led to the speculation that B-type olivine is also present in the Ryukyu Trench section.

2.8.2 The Nankai Trough and Kuril Trench

In the Nankai Trough section, the eastern part of the Philippine Sea plate is being subducted slightly off perpendicular to the trough. Most fast axes in this area are aligned in the same direction as plate subduction. The Philippine Sea plate is only ~15 m.y. old, meaning it probably has not cooled enough for the presence of B-type olivine. The lack of volcanoes close to this trench also suggests that the young, hot plate has a shallow dip and is not adding water to the overriding mantle. Even if there was enough water content, the plate is likely too hot for B-type olivine to form. Since it is unlikely for B-type olivine to be present in the Nankai Trough, it is reasonable to assume only A-type olivine exists in this section. Because fast axes are mostly aligned with plate motion, the simple 2D corner flow model can explain mantle wedge flow.

The "Better Events" results for the Kuril Trench area have fast axes that are parallel to the subducting plate motion as well as fast axes roughly perpendicular to plate motion. The difference in this area compared to the Japan Trench and Ryukyu Trench is that opposing trends are happening about the same distance from the trench. This lack of variance in distance of trends does not fit any model described in this study. It may be that the area is too complex for the *Silver and Chan* [1991] method to resolve.

The "Best Events" results for the Kuril Trench show only fast axes that are nearly perpendicular to plate motion. For the same reason the *Long and Silver* [2008] model does not explain mantle flowing parallel to the trench near the Japan Trench, it cannot explain it for the

Kuril Trench. If this model was depicting mantle flow near the Kuril Trench and the Japan Trench, it would also depict mantle flow near the Nankai Trough, and it does not.

The Pacific plate is just as old near the Kuril Trench as the Japan Trench. The abundance of volcanoes near the Kuril Trench also suggests that the subduction angle is probably the same here as at the Japan Trench. If the subduction angle is the same, the higher than usual water content that *Karato* [2003] suggests is in the mantle wedge near the Japan Trench is most likely be found near the Kuril Trench as well. Based on "Best Events" results for the Japan Trench, it can be speculated that there is presence of B-type olivine near the Kuril Trench.

2.9 Conclusion

Using data collected through NIED's F-net stations, SWS of SKS and SKKS waves were used to calculate fast axes directions and delay times from seismic anisotropy located beneath Japan. Trench-parallel fast axis directions were found near the Ryukyu and Japan Trenches and trench-perpendicular directions further from the trenches. Presence of B-type olivine is believed to be the cause of the trench-parallel trends in these sections.

The Nankai Trough has a fast axes direction parallel to the direction of the subducting plate. The 2D corner flow model can describe asthenospheic counterflow in this area. The absence of B-type olivine is due to the young, hot plate subducting shallowly. Using only "Best Events" results for the Kuril Trench, fast axes directions align almost perpendicular to subducted plate motion. B-type olivine is likely the cause of fast axes directions.

The findings in this study suggest that the mantle wedge is flowing in a 2D corner flow fashion within each trench system. The presences or absences of B-type olivine in each system determines if fast axes align perpendicular or parallel to mantle flow directions.

2.10 Figures

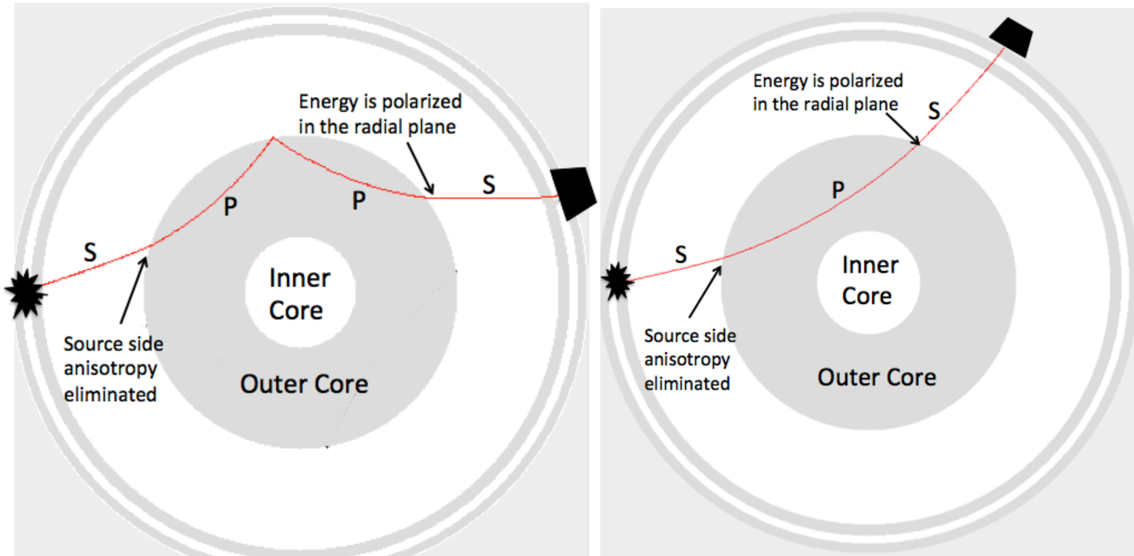

Figure 2.1: A sketch drawing of a cross section through the Earth. The starburst represents the earthquake, and the polygon is the receiver. a) The red line is the path of an SKS wave. As the wave is emitted from the hypocenter, it starts as an S-wave. When the wave hits the outer core it transforms its energy into a P-wave. After leaving the outer core, the wave turns back into an S-wave with its shear energy polarized in the radial plane. b) The red line is the path of an SKKS wave. An SKKS wave has a similar path of an SKS wave, but it bounces back into the outer core once before it reenters the mantle.

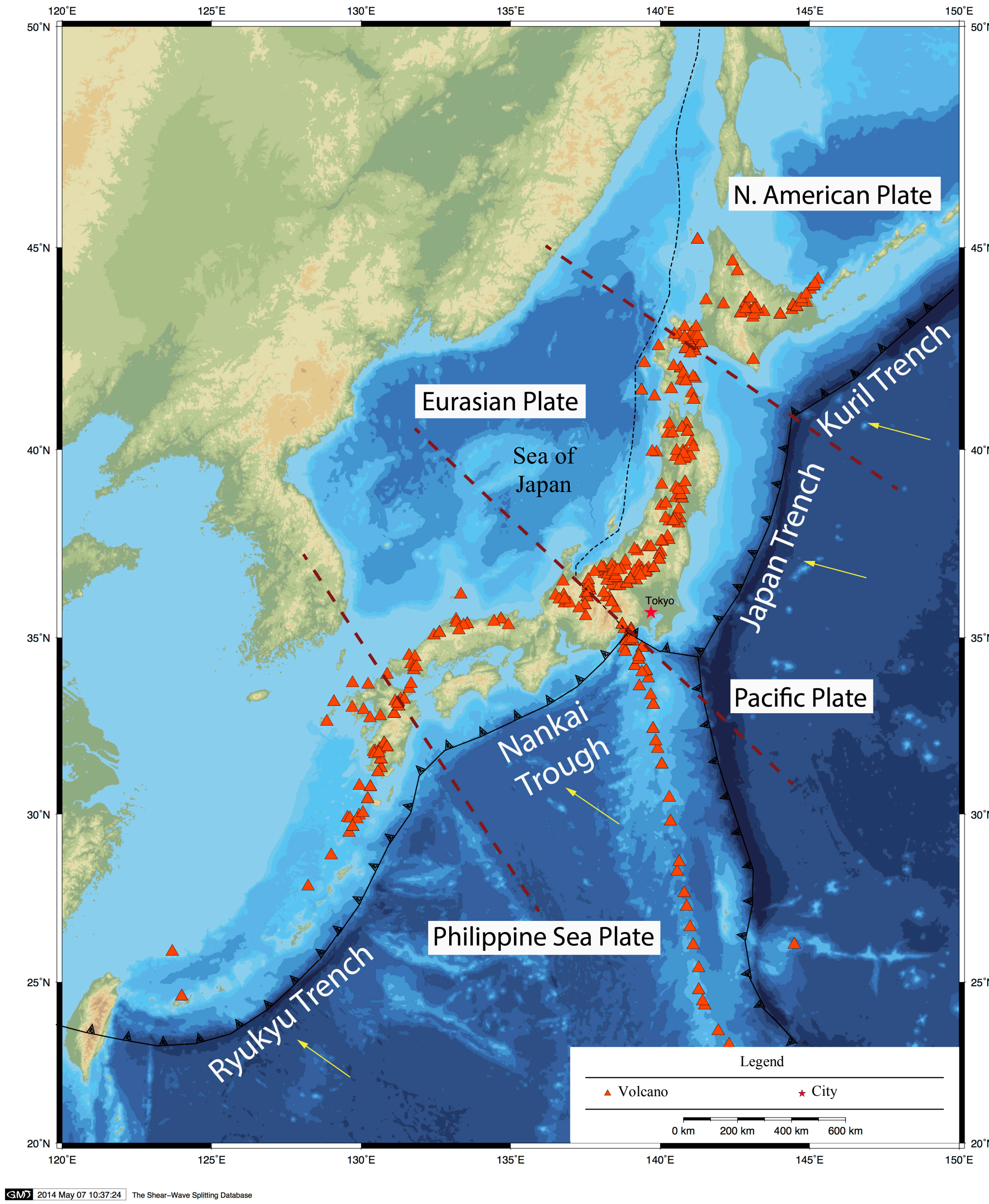

Figure 2.2: Tectonic map of the region around Japan. Northern Japan is a part of the Okhotsk plate that is a sometimes considered part of the North American plate. The southern part of Japan is a part of the Eurasia plate. Both the Pacific plate and the eastern part of Philippine plate are being subducted beneath Japan at rates of 90 mm/yr and 72 mm/yr respectively, while the western part of the Philippine plate is subducting at 79 mm/yr. There are two triple junctions located where the Pacific, Philippine Sea, and North America plates meet and where the Philippine Sea, North American, and Eurasia plates meet. Volcano locations were obtained from the Large Magnitude Explosive Volcanic Eruptions (LaMEVE) database [*Crosweller et al.*, 2012]. The black lines represent fault locations and the yellow arrows are relative plate motions from *Mahony et al.* [2011]. The dotted brown lines separate the different trenches based on plate motions and volcano locations.

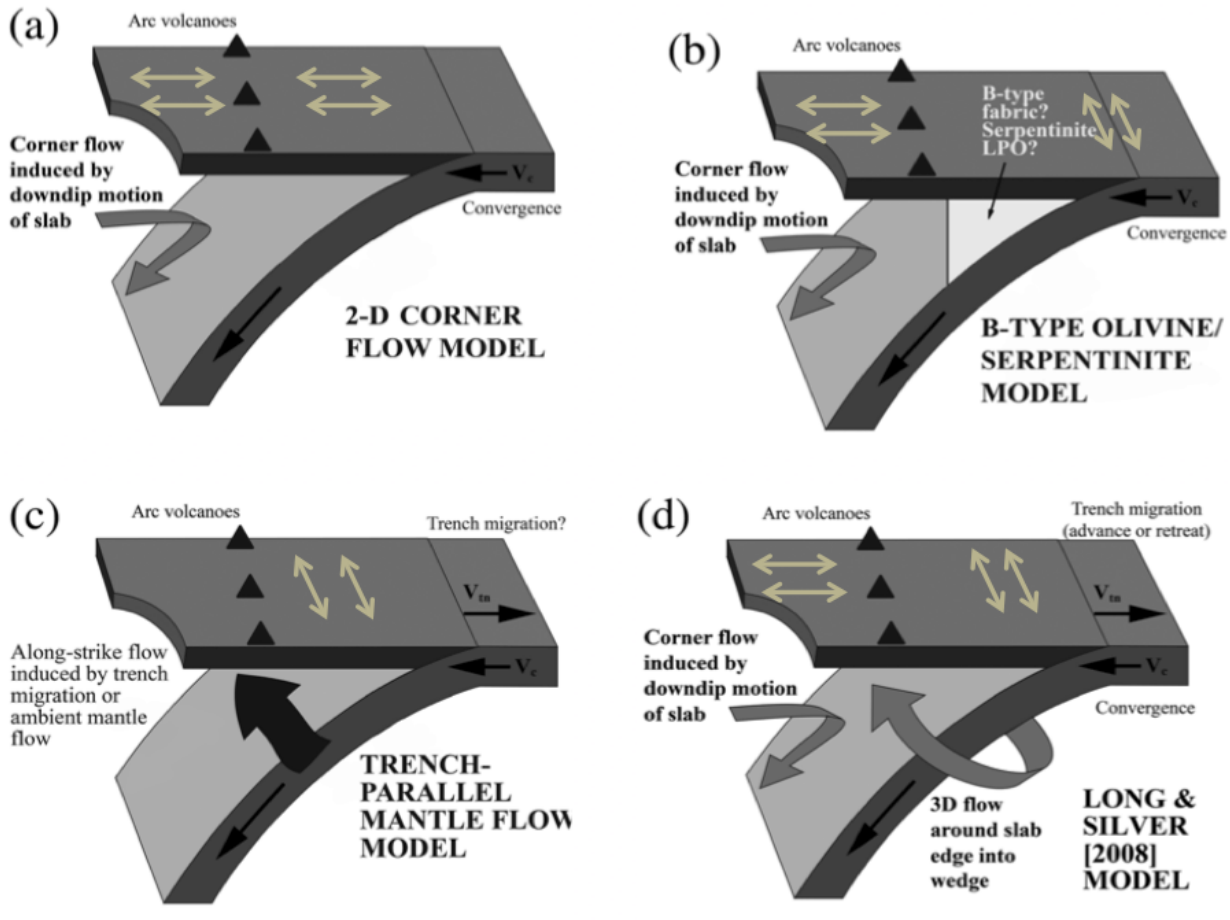

Figure 2.3: Cartoon sketches of mantle wedge flow models after *Long and Wirth* [2013]. The gold arrows on the surface represent fast axes orientations (a) 2-D Corner Flow Model assumes A-type olivine fabric and predicts trench-perpendicular anisotropy. (b) B-type Olivine Model has a high water content to produce B-type olivine close to the trench producing trench-parallel anisotropy while corner flow down dip produces trench-perpendicular anisotropy due to A-type olivine. (c) Trench-Parallel Mantle Flow Model has subslab mantle being pushed around the slab to cause trench-parallel mantle flow. (d) *Long and Silver* [2008] model is the combination of the Trench-Parallel Mantle Flow Model which produces near trench-parallel anisotropy while corner flow down dip produces trench-perpendicular anisotropy.

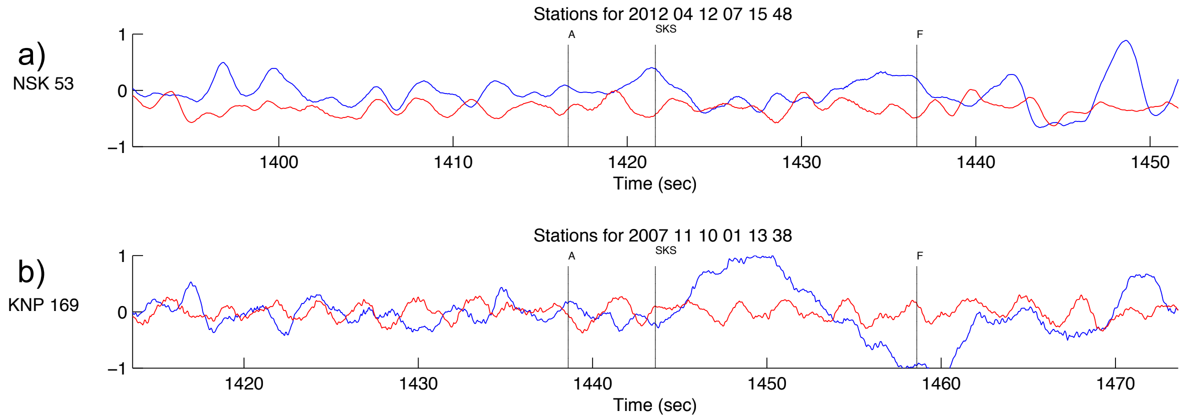

Figure 2.4: Examples of seismograms that passed and did not pass the first visual inspection. The blue line is the radial component and the red line is the transverse component. The station abbreviation and back azimuth are located to the left of the record sections. The SKS label represents the PREM model's expected arrival time of an SKS event. The A label represents 5 seconds before the wave arrival while the F label is 15 seconds after the wave arrival. The 20 second window between the A and F label defines the signal. Anything before the A label is noise. Anything after the F label was ignored. Record sections similar to a) were removed from the data set as there was not apparent SKS arrival. Record sections similar to b) were kept in the data set.

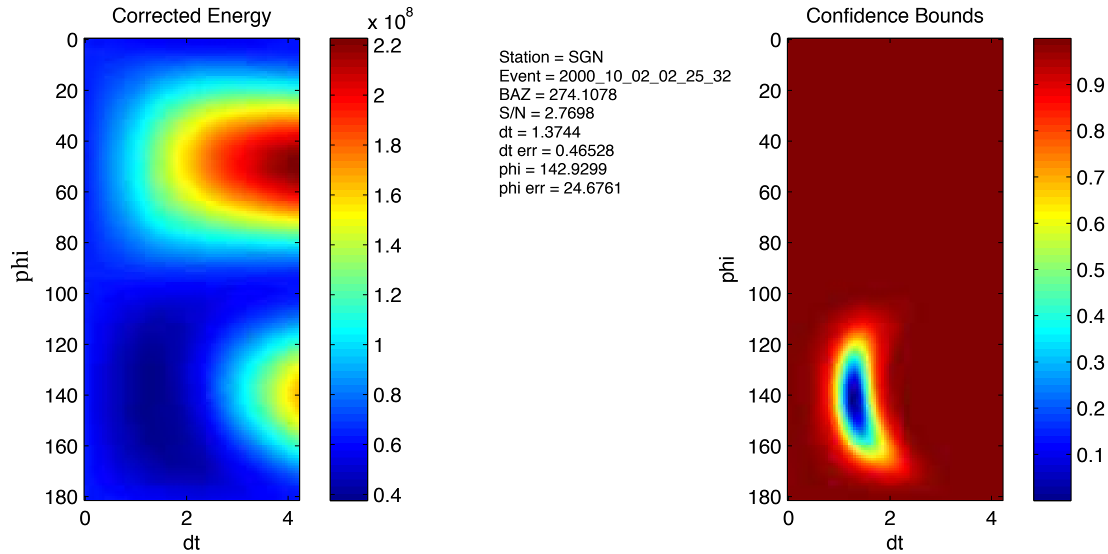

Figure 2.5: An example of a corrected energy plot (left) and confidence bounds (right) plot produced from *Silver and Chan* [1991]. The corrected energy plots the remaining transverse energy for each splitting pair searched. The lowest amount of corrected energy is presumed to be the best fitting fast axis polarization and delay time. The confidence bounds plot maps the probability density function as a function of splitting parameters. These are derived from the corrected tangential energy via the F-test, as described by *Silver and Chan* [1991].

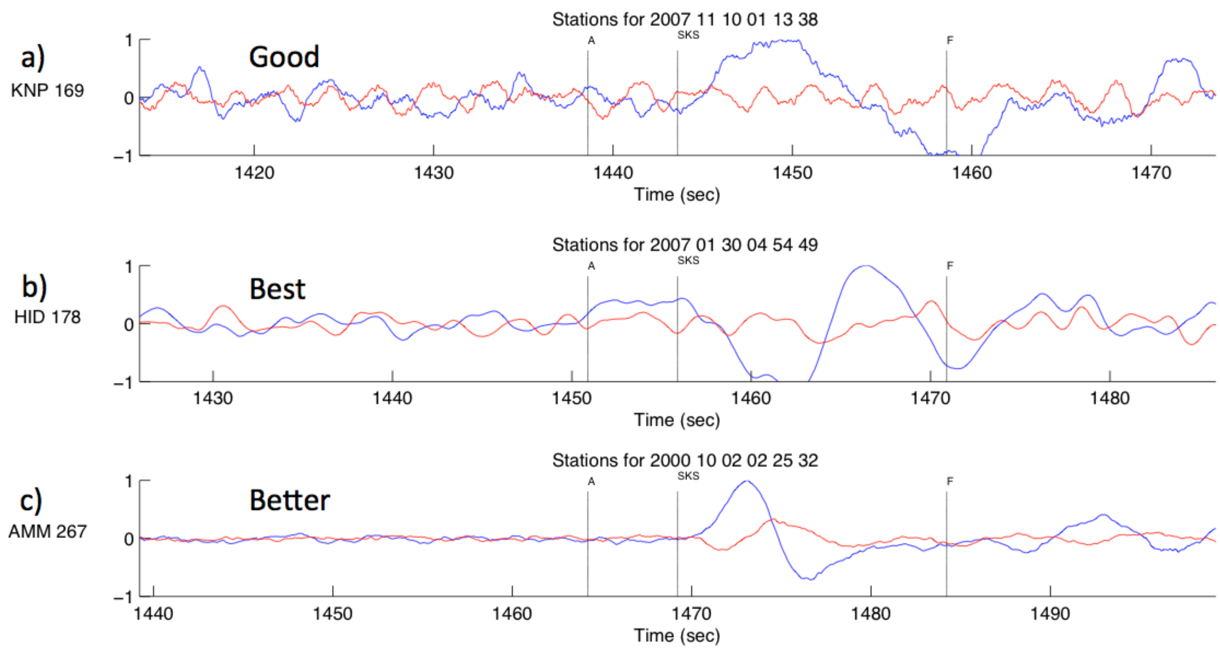

Figure 2.6: Example of seismograms for each event group. The blue line is the radial component and the red line is the transverse component. The station abbreviation and back azimuth are located to the left of the record sections. The SKS label represents the PREM's model expected arrival time of an SKS event. The A label represents 5 seconds before the wave arrival while the F label is 15 seconds after the wave arrival. The 20 second window between the A and F label defines the signal. Anything before the A label is noise. Anything after the F label was ignored. Seismograms similar to a) were deemed acceptable for events in "Good Events." Seismograms similar to b) were deemed acceptable for events in "Better Events." Seismograms similar to c) were deemed acceptable for events in "Best Events."

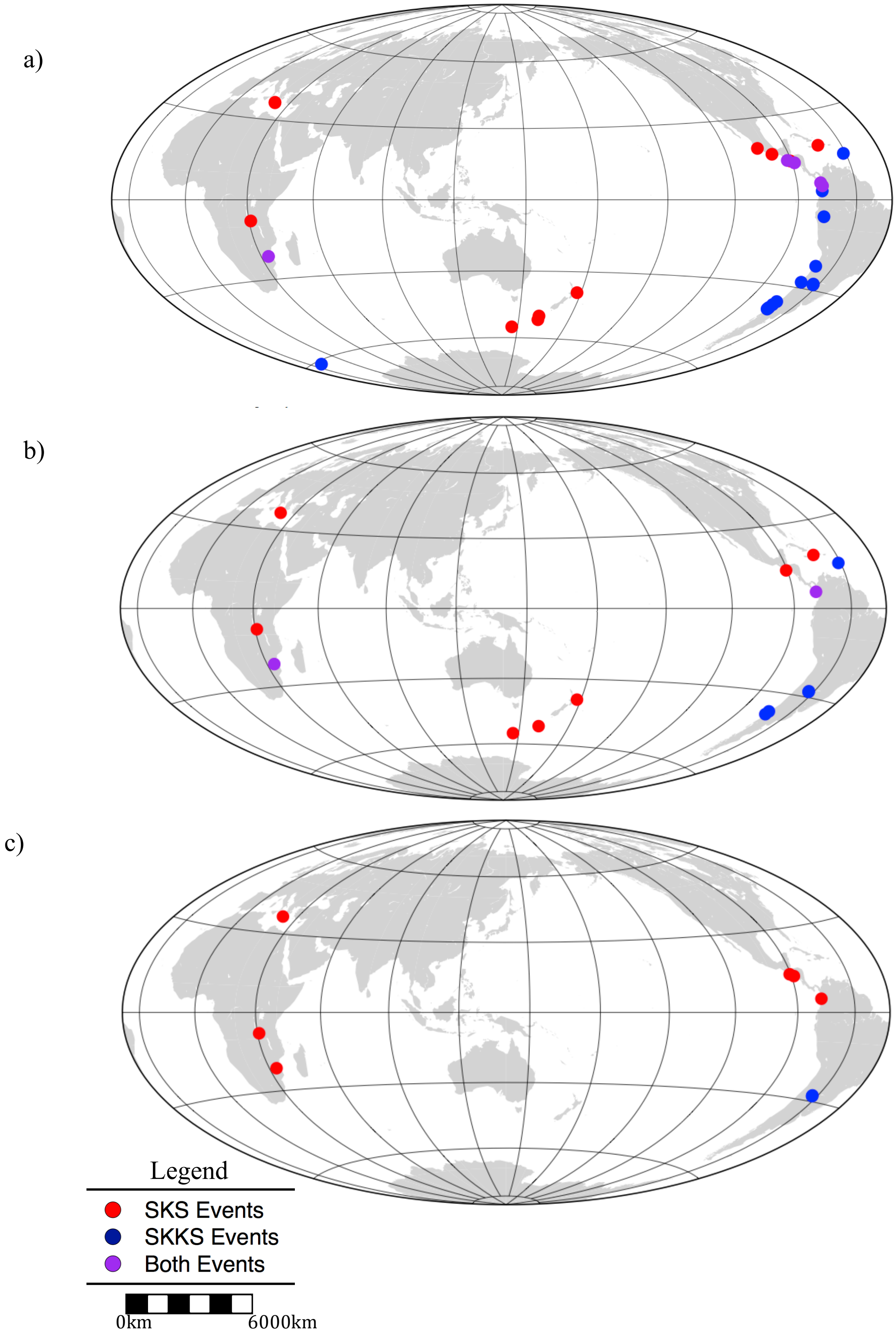

Figure 2.7: Event locations of for the three data groups. a) Good Events b) Better Events c) Best Events

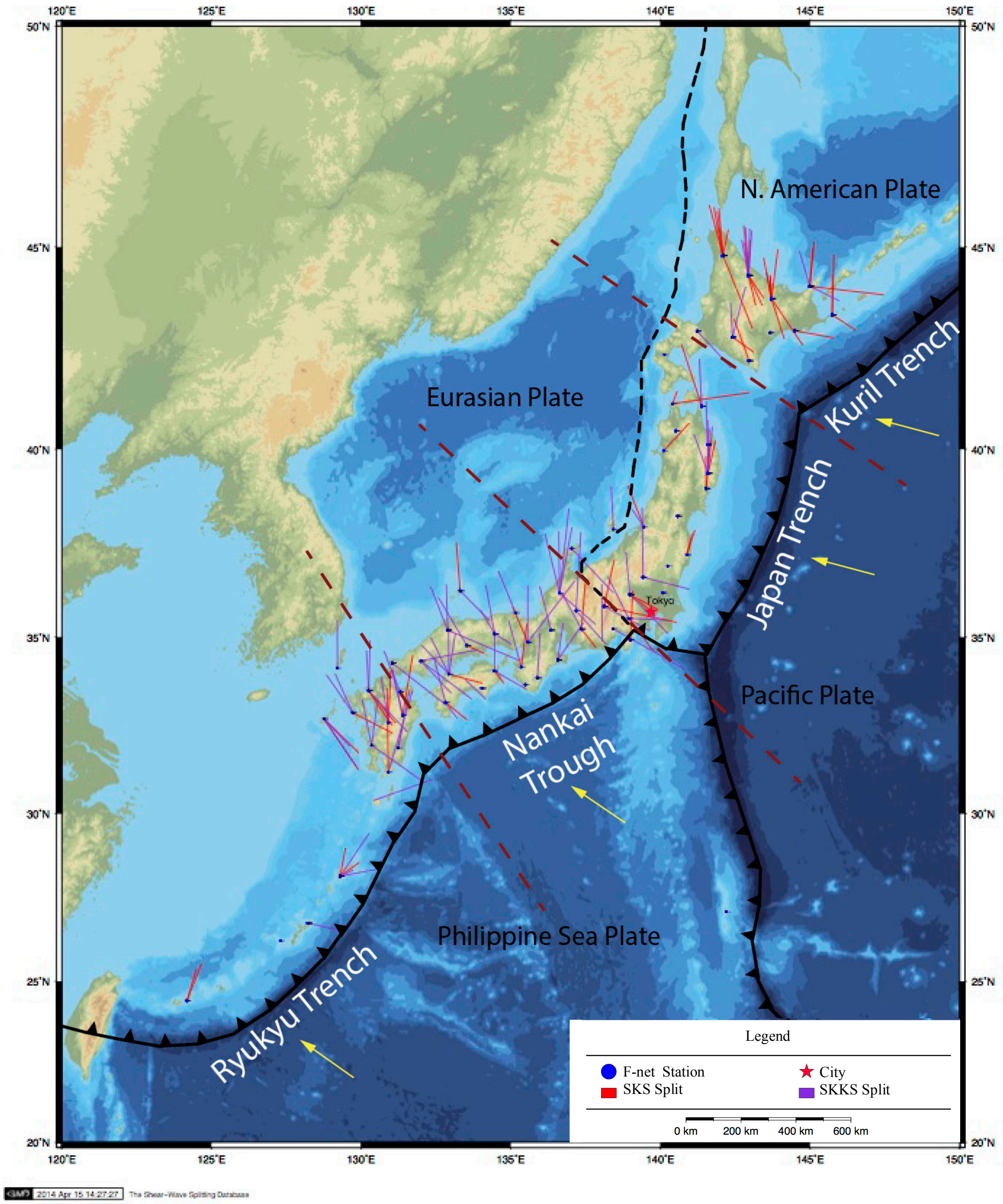

Figure 2.8: A map showing “Good Events” results. The orientations of the lines represent fast axis directions while the length corresponds to delay time. The black lines represent fault locations and the yellow arrows are relative plate motions from *Mahony et al.* [2011]. The dotted brown lines separate the different trenches based on plate motions and volcano locations.

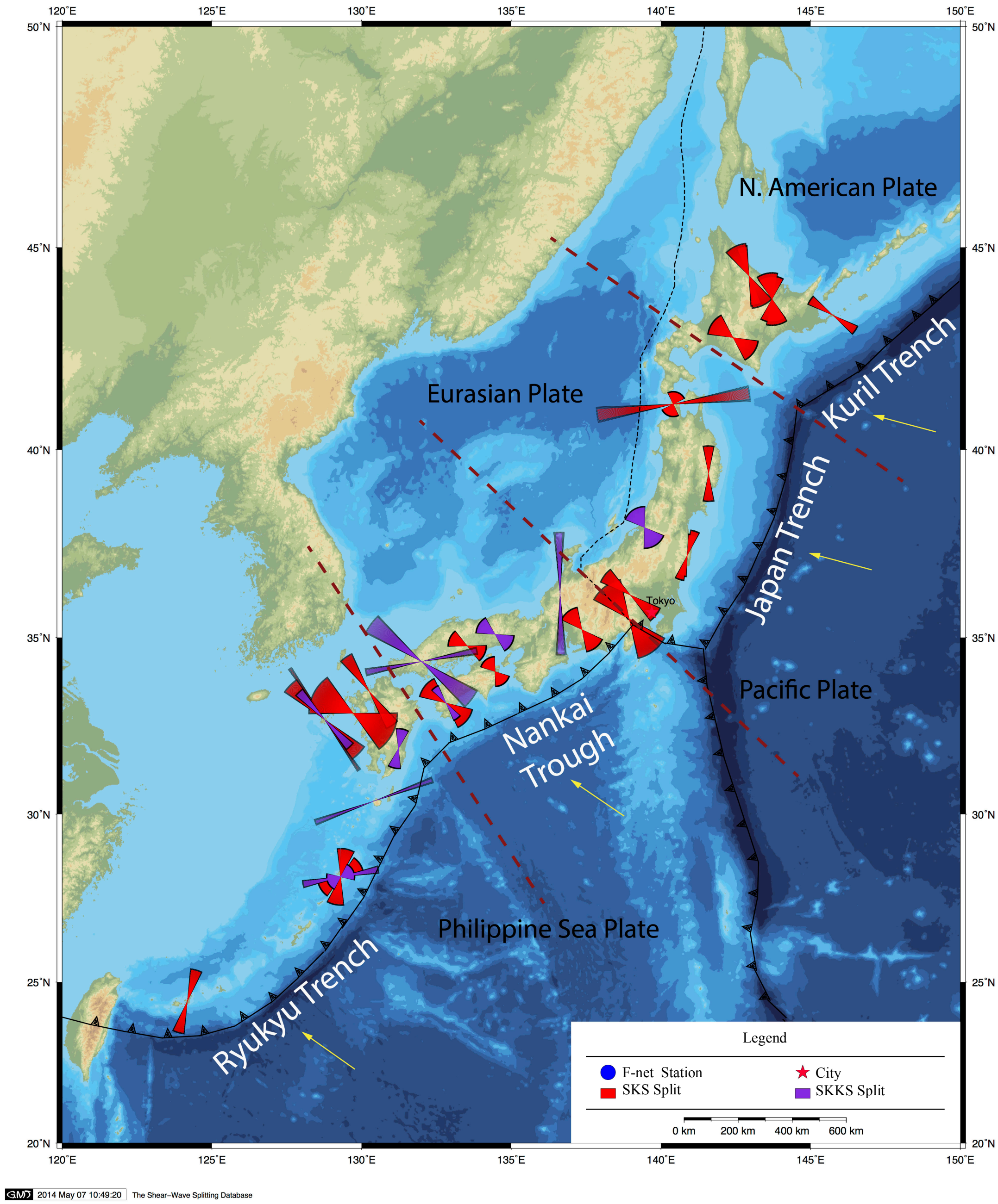

Figure 2.9: A map showing "Better Events" results. The orientations of the hourglass symbols represent the fast axis directions and the width of the symbols represents the amount of error. The length of the hourglass symbols represents the delay time. The black lines represent fault locations and the yellow arrows are relative plate motions from *Mahony et al.* [2011]. The dotted brown lines separate the different trenches based on plate motions and volcano locations.

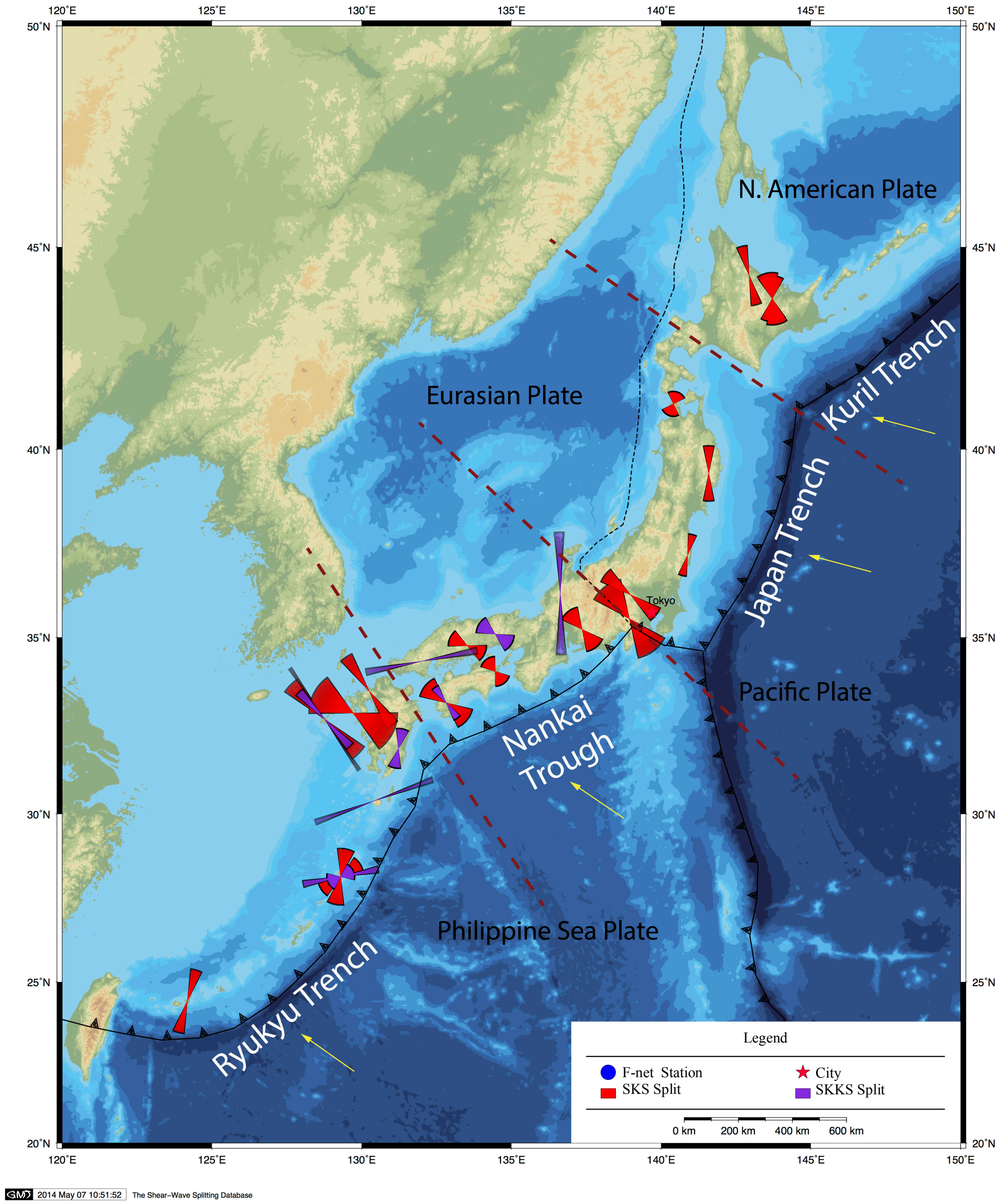

Figure 2.10: A map showing "Best Events" results. The orientations of the hourglass symbols represent the fast axis directions and the width of the symbols represents the amount of error. The length of the hourglass symbols represents the delay time. The black lines represent fault locations and the yellow arrows are relative plate motions from *Mahony et al.* [2011]. The dotted brown lines separate the different trenches based on plate motions and volcano locations.

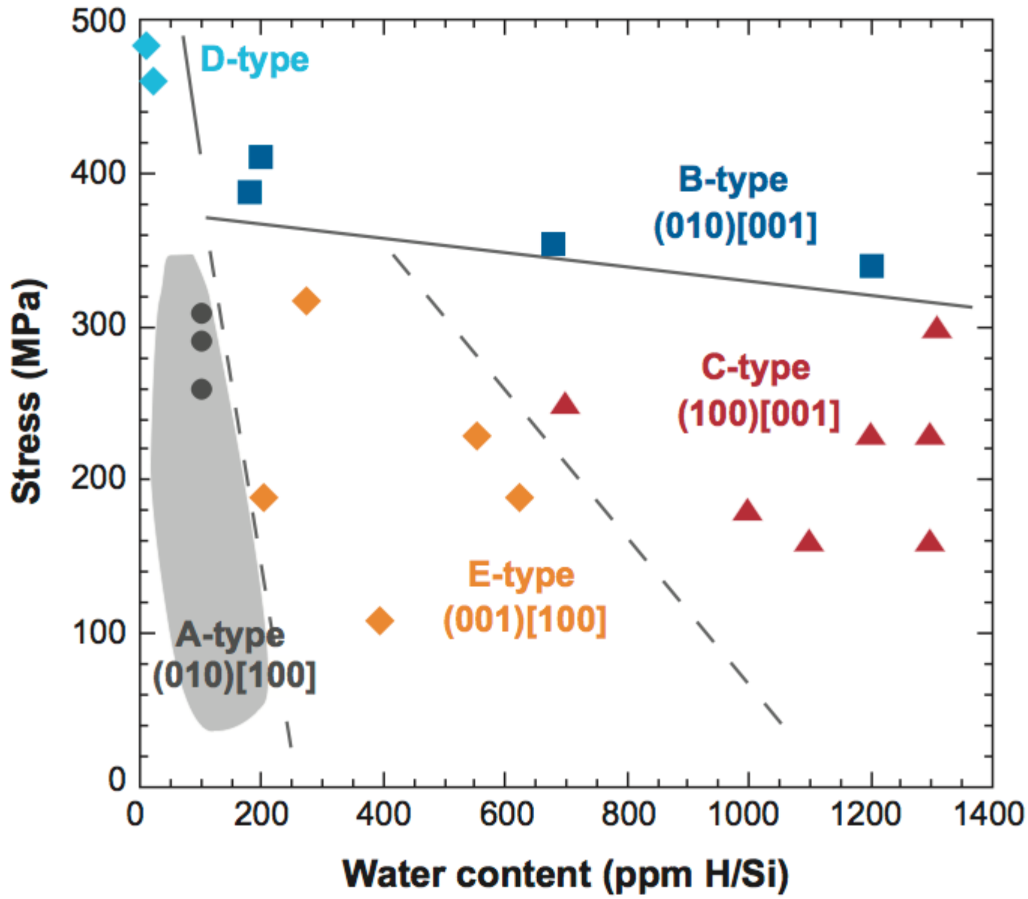

Figure 2.11: A plot of water content versus stress of olivine fabric types from *Karato et al.,* [2008].

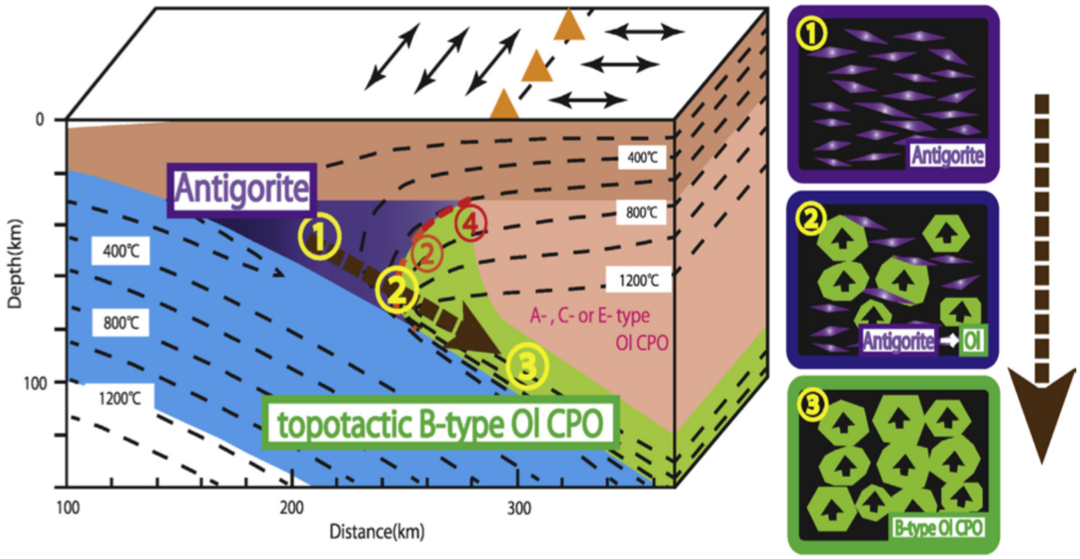

Figure 2.12: An illustration of possible B-type olivine distribution in subduction zones. The purple area indicates the zone of antigorite stability while the green represents where antigorite is expected to break down to olivine. The pictures on the right demonstrate this process. The brown and pink areas are continental crust and lithosphere where A-type (or C- or E-type) olivine is present. The blue area is the subducting oceanic crust. The dashed lines represent the calculated thermal structure of a subduction zone based on data from the Japan Trench. The triangles represent volcanoes. The arrows on the surface represent SWS directions [*Nagaya et al.,* 2014].

2.11 Tables

Table 2.1: A table of NIED F-net station information for stations used in this study.

Station	Code	Latitude	Longitude	Sensor	Start Date	End Date	Number of Seismograms		
							Good	Better	Best
Abuyama	ABU	34.8635N	135.5706E	STS-1	3/28/1998		3	0	0
Akadomari	ADM	37.9046N	138.4303E	STS-2.5	3/14/2002		1	0	0
Amamioshima	AMM	28.1571N	129.3001E	STS-1	3/20/1999		5	4	4
Ashio	ASI	36.6342N	139.4206E	STS-2	3/17/2001		2	0	0
Fujigawa	FUJ	35.2307N	138.4181E	STS-1	6/22/1996		1	0	0
Fukue	FUK	32.7177N	128.7572E	STS-1	6/22/1999		4	3	3
Gojome	GJM	39.9555N	140.1113E	STS-1	11/22/1997		1	0	0
Hidaka	HID	42.8208N	142.4145E	STS-2	12/29/2000		3	1	0
Hirono	HRO	37.2246N	140.8777E	STS-2	5/20/2000		2	2	1
Sapporo	HSS	42.9672N	141.2286E	STS-1	9/14/1996		1	0	0
Ishigaki	IGK	24.4131N	124.1808E	STS-2	5/20/2000		2	1	1
Nakatsu	INN	33.4701N	131.3062E	STS-2	2/24/2001		1	0	0
Tokushima	ISI	34.0606N	134.4554E	STS-2	3/9/1996		3	1	1
Yamagata	IYG	40.1217N	141.5833E	STS-2	1/20/2000		1	0	0
Izuhara	IZH	34.1359N	129.2066E	STS-2.5	2/17/2001		1	0	0
Nakaizu	JIZ	34.9167N	138.9938E	STS-2.5	3/17/1995		1	0	0
Kunigami	KGM	26.7567N	128.2153E	STS-2	2/25/2000		1	0	0
Kiwa	KIS	33.8652N	135.8907E	STS-1	3/7/1996		1	0	0
Kamikineusu	KMU	42.2391N	142.9625E	STS-2	2/8/2000		1	0	0
Kanayama	KNM	35.7168N	137.1781E	STS-2	4/14/2001		2	0	0
Kunneppu	KNP	43.7625N	143.7084E	STS-2	12/15/2000		7	2	2
Kanaya	KNY	34.8738N	138.0628E	STS-2	4/7/2001		1	0	0
Kesennuma	KSN	38.9762N	141.5301E	STS-2	2/11/2000		2	0	0
Kushiro	KSR	42.9820N	144.4851E	STS-2	12/13/2002		1	0	0
Nagata	KYK	30.3781N	130.4099E	STS-2	2/2/2001		1	1	1
Minmaya	MMA	41.1619N	140.4107E	STS-2	5/25/2001	5/31/2011	2	2	1
Asahi	NAA	35.2239N	137.3622E	STS-1	2/22/1997		3	1	1
Nakagawa	NKG	44.8017N	142.0849E	STS-2	12/14/2001		5	0	0
Nemuro	NMR	43.3673N	145.7379E	STS-2.5	8/19/1996		3	1	0
Nokami	NOK	34.1656N	135.3478E	STS-2	1/13/2001		2	0	0
Nishiokoppe	NOP	44.3218N	142.9384E	STS-2	12/6/2002		10	2	1
Nariwa	NRW	34.7682N	133.5325E	STS-2	5/12/2000		2	1	1
Nishiki	NSK	34.3403N	132.0018E	STS-2	4/21/2001		3	2	1
Ookawa	OKW	33.8272N	133.4691E	STS-1	6/9/2005		1	0	0
Onishi	ONS	36.1557N	138.9822E	STS-2	11/12/1999		4	1	1

Station	Code	Latitude	Longitude	Sensor	Start Date	End Date	Number of Seismograms		
							Good	Better	Best
Saigo	SAG	36.2553N	133.3050E	STS-2	2/22/2002		2	0	0
Sefuri	SBR	33.5052N	130.2530E	STS-1	2/6/1999		5	1	1
Shibata	SBT	37.9683N	139.4501E	STS-1	12/13/1997		2	1	0
Turusugeno	SGN	35.5096N	138.9444E	STS-1	3/17/1995		3	1	1
Shari	SHR	44.0563N	144.9944E	STS-2	12/21/2001		5	0	0
Shibisan	SIB	31.9698N	130.3486E	STS-2	1/15/2002		3	0	0
Shiramine	SRN	36.2018N	136.6303E	STS-2	11/14/2002		5	1	1
Sotome	STM	32.8870N	129.7237E	STS-2	1/31/2003		3	1	1
Tashiro	TAS	31.1946N	130.9093E	STS-2	1/20/2001		2	0	0
Taga	TGA	35.1847N	136.3383E	STS-2	4/21/2001		1	0	0
Tamagawa	TGW	33.9734N	132.9319E	STS-2	12/21/2000		5	0	0
Takeda	TKD	32.8179N	131.3875E	STS-2.5	3/9/1996		3	0	0
Takaoka	TKO	31.8931N	131.2321E	STS-2	3/3/2001		2	1	1
Tomochi	TMC	32.6063N	130.9151E	STS-2	1/26/2001		2	0	0
Tomari	TMR	41.1016N	141.3831E	STS-1	11/15/1997		2	0	0
Nakagawa	TNK	44.7779N	142.0791E	STS-1	9/16/1996	9/16/2004	1	0	0
Nishitosa	TSA	33.1781N	132.8200E	STS-2	3/23/2000		3	2	2
Takato	TTO	35.8363N	138.1209E	STS-1	4/10/1999		3	0	0
Tonoyamasaki	TYS	39.3772N	141.5932E	STS-2	1/11/2002		6	1	1
Wajima	WJM	37.4021N	137.0257E	STS-2	12/19/2003		1	0	0
Watarai	WTR	34.3739N	136.5748E	STS-2	4/7/2001		2	0	0
Yasaka	YAS	35.6570N	135.1605E	STS-2	3/24/2001		1	0	0
Yoshida	YSI	35.1942N	132.8862E	STS-2	3/30/2001		3	0	0
Toyota	YTY	34.2835N	131.0364E	STS-2	4/21/2000		1	0	0
Yamasaki	YZK	35.0888N	134.4594E	STS-2	4/21/2000		3	1	1
						Total	**153**	**35**	**28**

Table 2.2: A list of events used in this study.
Latitude and Longitude are given such that positive is north and east and negative is south and west respectively.

Event Date (YYYY_MM_DD_HH_MM_SS)	Latitude	Longitude	Magnitude Mw	Number of Seismograms Good	Better	Best
2000_04_23_09_27_23	-28.289	-62.944	7	2	2	2
2000_10_02_02_25_32	-7.845	30.817	6.5	14	10	10
2001_01_13_17_33_34	12.997	-88.729	7.6	6	1	1
2004_05_03_04_36_47	-37.806	-73.416	6.6	7	0	0
2004_11_15_09_06_55	4.742	-77.470	7.2	7	1	0
2004_12_23_14_59_00	-49.710	161.576	8	1	0	0
2005_09_26_01_55_37	-5.736	-76.476	7.5	2	0	0
2006_01_02_06_10_48	-61.011	-21.649	7.1	2	0	0
2006_02_22_22_19_09	-21.311	33.549	7	20	3	3
2007_01_30_04_54_49	-54.917	146.290	6.9	6	1	0
2007_06_13_19_29_46	13.716	-90.570	6.7	5	4	4
2007_09_10_01_49_14	3.000	-77.900	6.8	6	0	0
2007_11_10_01_13_38	-51.418	161.602	6.6	3	0	0
2007_11_14_15_40_49	-22.321	-69.780	7.7	1	0	0
2007_11_29_19_00_19	14.995	-61.224	7.4	1	1	0
2007_12_20_07_55_19	-38.948	178.012	6.7	1	1	0
2008_02_14_10_09_23	36.517	21.670	6.9	2	2	1
2010_01_12_21_53_10	18.382	-72.588	7	3	1	0
2010_03_05_11_47_07	-36.667	-73.449	6.6	5	1	0
2010_07_14_08_32_21	-38.063	-73.465	6.6	6	0	0
2011_01_02_20_20_18	-38.391	-73.399	7.1	27	0	0
2011_02_14_03_40_09	-35.487	-73.101	6.6	1	0	0
2012_03_20_18_02_47	16.493	-98.231	7.4	4	0	0
2012_05_28_05_07_23	-28.043	-63.094	6.7	8	7	7
2012_11_07_16_35_46	13.988	-91.895	7.3	6	0	0
2013_01_30_20_15_43	-28.094	-70.653	6.8	2	0	0
2013_08_13_15_43_15	5.773	-78.200	6.7	5	0	0
		Total		**153**	**35**	**28**
		Total Number of Events		**27**	**13**	**7**

Table 2.3: A list of "Good Events" results.

Stn	Event Date YYYY_MM_DD_HH_MM_SS	Back Azimuth (°)	SNR	δt (s)	δt Error (s)	ϕ (°)	ϕ Error (°)	Phase
ABU	2000_10_02_02_25_32	271.92	3.42	1.29	2.10	-23.27	45.00	SKS
ABU	2005_09_26_01_55_37	52.97	2.87	1.91	2.10	-0.14	45.00	SKKS
ABU	2007_09_10_01_49_14	46.82	2.89	2.57	1.53	37.28	6.43	SKKS
ADM	2011_01_02_20_20_18	101.03	3.04	1.44	2.10	-2.94	45.00	SKKS
AMM	2000_10_02_02_25_32	267.01	5.26	0.80	0.33	54.06	19.94	SKS
AMM	2006_02_22_22_19_09	253.48	4.43	0.97	0.46	10.66	17.52	SKS
AMM	2000_04_23_09_27_23	93.58	2.73	0.49	0.77	64.59	39.43	SKKS
AMM	2012_05_28_05_07_23	92.32	3.10	1.30	0.46	79.20	5.51	SKKS
AMM	2012_11_07_16_35_46	49.04	3.16	1.75	2.10	33.80	23.11	SKKS
ASI	2007_11_14_15_40_49	68.66	2.80	1.60	1.74	104.53	44.97	SKKS
ASI	2013_01_30_20_15_43	80.08	2.69	2.32	1.26	-0.75	7.64	SKKS
FUJ	2011_01_02_20_20_18	106.51	2.78	2.73	1.50	119.61	10.12	SKKS
FUK	2000_10_02_02_25_32	267.63	6.06	2.07	0.11	146.09	1.66	SKS
FUK	2006_02_22_22_19_09	254.41	5.23	1.64	0.47	134.63	11.06	SKS
FUK	2011_01_02_20_20_18	113.66	3.95	1.95	1.21	146.23	25.30	SKKS
FUK	2012_05_28_05_07_23	68.61	2.94	1.27	0.38	137.07	8.20	SKKS
GJM	2001_01_13_17_33_34	51.58	3.16	1.27	0.81	42.61	8.27	SKS
HID	2007_01_30_04_54_49	177.75	3.00	0.87	0.43	125.30	28.32	SKS
HID	2006_02_22_22_19_09	266.00	3.13	1.15	2.10	-3.18	45.00	SKKS
HID	2011_01_02_20_20_18	92.92	2.82	1.75	2.10	14.32	45.00	SKKS
HRO	2008_02_14_10_09_23	315.27	3.26	0.73	0.23	14.35	12.27	SKS
HRO	2008_02_14_12_08_57	315.08	2.58	0.87	0.27	17.88	10.72	SKS
HSS	2006_02_22_22_19_09	265.31	3.14	1.67	1.57	137.33	43.07	SKKS
IGK	2000_10_02_02_25_32	264.24	5.09	1.12	0.46	16.36	10.51	SKS
IGK	2006_02_22_22_19_09	250.77	3.74	1.33	2.10	21.35	45.00	SKS
INN	2011_01_02_20_20_18	110.85	3.25	1.48	2.10	-21.54	45.00	SKKS
ISI	2000_10_02_02_25_32	271.05	5.53	0.52	0.32	142.76	35.95	SKS
ISI	2001_01_13_17_33_34	48.91	3.74	1.37	2.10	0.08	45.00	SKKS
ISI	2004_05_03_04_36_47	107.45	2.89	1.23	0.85	119.95	10.41	SKKS
IYG	2006_02_22_22_19_09	264.09	2.88	1.44	2.10	-1.96	45.00	SKKS
IZH	2007_09_10_01_49_14	40.14	2.70	1.62	2.10	-0.25	45.00	SKKS
JIZ	2006_02_22_22_19_09	260.19	3.17	1.65	2.10	3.06	45.00	SKS
KGM	2007_09_10_01_49_14	44.46	3.11	1.12	1.57	102.18	45.42	SKKS
KIS	2001_01_13_17_33_34	50.18	2.86	1.49	2.10	3.45	45.00	SKKS
KMU	2006_02_22_22_19_09	266.05	3.32	1.49	2.10	-19.48	45.00	SKS
KNM	2004_05_03_04_36_47	104.00	2.86	1.52	0.82	138.18	23.19	SKKS
KNM	2011_01_02_20_20_18	105.40	3.23	2.64	1.07	3.50	7.63	SKKS
KNP	2001_01_13_17_33_34	53.51	6.52	0.79	0.61	-3.14	33.00	SKS
KNP	2006_02_22_22_19_09	267.36	3.70	1.39	2.10	-10.88	45.00	SKS

Stn	Event Date YYYY_MM_DD_HH_MM_SS	Back Azimuth (°)	SNR	δt (s)	δt Error (s)	ϕ (°)	ϕ Error (°)	Phase
KNP	2007_01_30_04_54_49	178.49	4.22	1.41	1.51	162.51	19.88	SKS
KNP	2007_06_13_19_29_46	54.55	3.16	0.90	0.79	-10.67	24.10	SKS
KNP	2007_11_10_01_13_38	168.84	2.65	1.67	2.10	7.37	45.00	SKS
KNP	2010_01_12_21_53_10	36.68	3.35	1.88	1.88	146.11	19.77	SKS
KNP	2013_08_13_15_43_15	48.75	2.72	0.76	0.89	-3.53	45.00	SKS
KNY	2004_05_03_04_36_47	105.85	2.70	1.93	1.87	-0.57	19.45	SKKS
KSN	2001_01_13_17_33_34	53.01	4.17	1.09	1.00	-0.51	40.44	SKS
KSN	2012_11_07_16_35_46	54.82	2.68	1.61	2.10	4.90	45.00	SKS
KSR	2007_01_30_04_54_49	178.95	3.20	1.32	1.18	100.41	12.14	SKS
KYK	2012_05_28_05_07_23	82.19	2.98	2.10	0.40	70.21	2.90	SKKS
MMA	2007_06_13_19_29_46	52.52	2.67	0.44	0.53	19.06	45.00	SKS
MMA	2007_12_20_07_55_19	151.54	2.54	2.59	0.64	81.72	5.68	SKS
NAA	2000_10_02_02_25_32	273.07	3.79	0.78	0.32	142.13	26.93	SKS
NAA	2012_03_20_18_02_47	55.59	3.18	1.55	2.10	4.85	45.00	SKS
NAA	2010_07_14_08_32_21	105.67	3.00	1.38	2.10	-28.43	45.00	SKKS
NKG	2004_12_23_14_59_00	167.43	3.26	1.59	2.10	-4.79	45.00	SKS
NKG	2007_01_30_04_54_49	177.54	2.74	2.64	0.81	158.07	7.04	SKS
NKG	2007_06_13_19_29_46	53.02	2.79	1.75	2.10	-15.08	45.00	SKS
NKG	2010_01_12_21_53_10	35.00	2.78	1.63	2.10	-10.65	45.00	SKS
NKG	2012_11_07_16_35_46	53.93	3.67	0.88	0.52	11.69	31.39	SKS
NMR	2004_11_15_09_06_55	50.78	2.77	0.93	0.46	123.57	10.98	SKS
NMR	2007_11_10_01_13_38	170.10	2.57	2.01	2.10	1.56	45.00	SKS
NOK	2006_02_22_22_19_09	258.06	3.96	1.47	2.10	7.32	45.00	SKS
NOK	2004_05_03_04_36_47	107.20	2.80	1.60	2.10	-15.08	45.00	SKKS
NOP	2004_11_15_09_06_55	47.73	3.08	1.11	1.23	-6.66	42.86	SKS
NOP	2007_01_30_04_54_49	178.04	4.10	0.92	1.01	146.14	41.68	SKS
NOP	2007_06_13_19_29_46	53.81	2.76	1.03	0.39	166.14	10.81	SKS
NOP	2007_11_10_01_13_38	168.36	2.64	1.62	2.10	-3.64	45.00	SKS
NOP	2010_01_12_21_53_10	35.87	3.77	1.11	0.53	155.39	19.51	SKS
NOP	2013_08_13_15_43_15	47.80	2.77	1.20	1.83	2.75	45.00	SKS
NOP	2005_09_26_01_55_37	53.71	2.78	1.51	2.10	4.36	45.00	SKKS
NOP	2006_02_22_22_19_09	267.15	3.04	1.21	2.10	-10.43	45.00	SKKS
NOP	2011_01_02_20_20_18	90.39	2.90	1.69	2.10	-5.30	45.00	SKKS
NOP	2013_08_13_15_43_15	47.80	3.01	1.57	2.10	1.64	45.00	SKKS

Stn	Event Date YYYY_MM_DD_HH_MM_SS	Back Azimuth (°)	SNR	δt (s)	δt Error (s)	ϕ (°)	ϕ Error (°)	Phase
TGA	2011_01_02_20_20_18	106.46	3.43	1.52	2.10	-14.39	45.00	SKKS
TGW	2006_02_22_22_19_09	256.80	6.26	1.16	1.28	104.96	35.88	SKS
TGW	2007_09_10_01_49_14	44.54	2.86	1.59	2.10	-0.27	45.00	SKKS
TGW	2010_03_05_11_47_07	104.66	3.38	1.37	2.10	-25.95	45.00	SKKS
TGW	2011_01_02_20_20_18	109.32	3.58	1.33	1.90	-42.75	40.11	SKKS
TGW	2013_01_30_20_15_43	80.20	3.09	1.39	2.10	9.10	45.00	SKKS
TKD	2000_10_02_02_25_32	269.05	4.58	2.03	1.06	9.44	5.92	SKS
TKD	2010_07_14_08_32_21	111.50	2.69	1.58	2.10	-12.38	45.00	SKKS
TKD	2011_02_14_03_40_09	104.27	2.72	1.58	2.10	-13.38	45.00	SKKS
TKO	2011_01_02_20_20_18	114.68	4.19	2.01	2.09	11.34	15.28	SKKS
TKO	2012_05_28_05_07_23	76.51	2.98	0.70	0.41	11.75	19.37	SKKS
TMC	2006_02_22_22_19_09	255.40	4.44	1.74	1.84	2.72	20.28	SKS
TMC	2004_05_03_04_36_47	111.44	2.59	1.53	2.10	-8.98	45.00	SKKS
TMR	2012_03_20_18_02_47	57.31	2.84	2.17	2.04	-18.02	20.67	SKS
TMR	2011_01_02_20_20_18	95.70	2.71	1.58	2.10	-2.91	45.00	SKKS
TNK	2001_01_13_17_33_34	51.94	4.36	1.51	1.79	-6.83	40.08	SKS
TSA	2000_10_02_02_25_32	269.91	5.79	0.93	0.42	128.85	26.38	SKS
TSA	2000_04_23_09_27_23	74.40	2.75	0.66	0.35	143.76	12.75	SKKS
TSA	2011_01_02_20_20_18	111.21	3.10	1.54	2.10	-14.35	45.00	SKKS
TTO	2000_10_02_02_25_32	273.73	2.57	2.48	1.65	102.55	7.39	SKS
TTO	2012_03_20_18_02_47	55.98	3.27	1.60	1.34	12.17	45.00	SKS
TTO	2011_01_02_20_20_18	105.26	3.57	1.72	2.08	118.27	17.70	SKKS
TYS	2004_11_15_09_06_55	48.66	3.10	1.12	0.82	12.93	36.20	SKS
TYS	2007_06_13_19_29_46	53.92	2.76	0.95	0.23	0.50	11.71	SKS
TYS	2006_01_02_06_10_48	200.18	2.57	1.78	2.10	-0.36	45.00	SKKS
TYS	2006_02_22_22_19_09	263.72	2.71	1.57	2.10	5.25	45.00	SKKS
TYS	2010_07_14_08_32_21	98.48	2.87	1.39	2.10	-19.67	45.00	SKKS
TYS	2013_08_13_15_43_15	48.65	2.83	1.50	2.10	1.40	45.00	SKKS
WJM	2011_01_02_20_20_18	101.74	2.70	2.05	1.70	136.81	38.17	SKKS
WTR	2004_11_15_09_06_55	46.36	3.21	1.24	1.25	8.33	45.00	SKKS
WTR	2011_01_02_20_20_18	108.19	4.99	1.52	2.10	34.82	30.02	SKKS
YAS	2004_11_15_09_06_55	44.13	2.64	1.52	1.58	-22.02	25.86	SKKS
YSI	2007_09_10_01_49_14	43.70	3.09	1.53	2.10	-1.63	45.00	SKKS
YSI	2010_07_14_08_32_21	105.48	2.70	1.58	2.10	-21.21	45.00	SKKS
YSI	2011_01_02_20_20_18	106.38	3.95	2.59	1.82	113.10	5.67	SKKS
YTY	2011_01_02_20_20_18	108.85	3.33	2.30	1.98	127.99	14.41	SKKS
YZK	2004_05_03_04_36_47	105.10	2.57	1.65	2.10	-10.04	45.00	SKKS
YZK	2011_01_02_20_20_18	106.62	4.06	0.95	0.78	-30.46	45.00	SKKS
YZK	2012_05_28_05_07_23	69.68	3.94	0.66	0.37	122.19	29.18	SKKS

Table 2.4: A list of "Better Events" results

Stn	Event Date YYYY_MM_DD_HH_MM_SS	Back Azimuth (°)	SNR	δt (s)	δt Error (s)	ϕ (°)	ϕ Error (°)	Phase
AMM	2000_10_02_02_25_32	267.014	5.256	0.796	0.328	54.055	19.938	SKS
AMM	2006_02_22_22_19_09	253.479	4.434	0.967	0.455	10.66	17.522	SKS
FUK	2000_10_02_02_25_32	267.626	6.061	2.068	0.112	146.091	1.662	SKS
FUK	2006_02_22_22_19_09	254.412	5.233	1.644	0.466	134.626	11.056	SKS
HID	2007_01_30_04_54_49	177.745	3.002	0.874	0.43	125.296	28.323	SKS
HRO	2008_02_14_10_09_23	315.266	3.256	0.732	0.227	14.347	12.27	SKS
HRO	2008_02_14_12_08_57	315.08	2.575	0.867	0.273	17.883	10.72	SKS
IGK	2000_10_02_02_25_32	264.243	5.093	1.115	0.457	16.358	10.513	SKS
ISI	2000_10_02_02_25_32	271.051	5.531	0.523	0.32	142.755	35.951	SKS
KNP	2007_06_13_19_29_46	54.548	3.162	0.897	0.788	-10.668	24.095	SKS
KNP	2001_01_13_17_33_34	53.512	6.519	0.787	0.61	-3.137	32.996	SKS
MMA	2007_06_13_19_29_46	52.515	2.668	0.439	0.534	19.057	45	SKS
MMA	2007_12_20_07_55_19	151.541	2.537	2.591	0.636	81.722	5.684	SKS
NAA	2000_10_02_02_25_32	273.073	3.785	0.775	0.32	142.13	26.933	SKS
NMR	2004_11_15_09_06_55	50.779	2.768	0.927	0.463	123.566	10.982	SKS
NOP	2007_06_13_19_29_46	53.814	2.758	1.031	0.394	166.138	10.809	SKS
NOP	2010_01_12_21_53_10	35.871	3.772	1.108	0.531	155.394	19.512	SKS
NRW	2000_10_02_02_25_32	270.721	4.318	0.661	0.599	114.781	26.575	SKS
ONS	2000_10_02_02_25_32	274.355	2.846	1.109	0.342	128.194	14.759	SKS
SBR	2000_10_02_02_25_32	268.59	3.643	1.401	0.345	146.182	10.221	SKS
SGN	2000_10_02_02_25_32	274.108	2.77	1.374	0.465	142.93	24.676	SKS
STM	2006_02_22_22_19_09	254.918	6.831	1.5	0.645	117.233	28.315	SKS
TSA	2000_10_02_02_25_32	269.912	5.794	0.93	0.422	128.849	26.38	SKS
TYS	2007_06_13_19_29_46	53.919	2.761	0.952	0.233	0.495	11.712	SKS
AMM	2000_04_23_09_27_23	93.583	2.73	0.491	0.77	64.59	39.431	SKKS
AMM	2012_05_28_05_07_23	92.32	3.103	1.3	0.464	79.197	5.507	SKKS
FUK	2012_05_28_05_07_23	68.612	2.938	1.273	0.381	137.073	8.195	SKKS
KYK	2012_05_28_05_07_23	82.192	2.981	2.095	0.396	70.209	2.903	SKKS
NSK	2010_03_05_11_47_07	103.716	3.105	2.12	0.644	127.003	9.96	SKKS
NSK	2012_05_28_05_07_23	68.169	3.239	1.907	0.698	78.697	4.408	SKKS
SBT	2007_11_29_19_00_19	24.257	2.857	0.72	0.643	-33.476	35.271	SKKS
SRN	2012_05_28_05_07_23	69.589	3.759	2.07	0.488	-0.711	4.834	SKKS
TKO	2012_05_28_05_07_23	76.51	2.981	0.695	0.407	11.748	19.365	SKKS
TSA	2000_04_23_09_27_23	74.401	2.751	0.659	0.352	143.76	12.749	SKKS
YZK	2012_05_28_05_07_23	69.676	3.944	0.662	0.37	122.193	29.178	SKKS

Table 2.5: A list of “Best Events” results

Stn	Event Date YYYY_MM_DD_HH_MM_SS	Back Azimuth (°)	SNR	δt (s)	δt Error (s)	ϕ (°)	ϕ Error (°)	Phase
AMM	2000_10_02_02_25_32	267.014	5.256	0.796	0.328	54.055	19.938	SKS
AMM	2006_02_22_22_19_09	253.479	4.434	0.967	0.455	10.66	17.522	SKS
AMM	2000_04_23_09_27_23	93.583	2.73	0.491	0.77	64.59	39.431	SKKS
AMM	2012_05_28_05_07_23	92.32	3.103	1.3	0.464	79.197	5.507	SKKS
FUK	2000_10_02_02_25_32	267.626	6.061	2.068	0.112	146.091	1.662	SKS
FUK	2006_02_22_22_19_09	254.412	5.233	1.644	0.466	134.626	11.056	SKS
FUK	2012_05_28_05_07_23	68.612	2.938	1.273	0.381	137.073	8.195	SKKS
HRO	2008_02_14_10_09_23	315.266	3.256	0.732	0.227	14.347	12.27	SKS
IGK	2000_10_02_02_25_32	264.243	5.093	1.115	0.457	16.358	10.513	SKS
ISI	2000_10_02_02_25_32	271.051	5.531	0.523	0.32	142.755	35.951	SKS
KNP	2001_01_13_17_33_34	53.512	6.519	0.787	0.61	-3.137	32.996	SKS
KNP	2007_06_13_19_29_46	54.548	3.162	0.897	0.788	-10.668	24.095	SKS
KYK	2012_05_28_05_07_23	82.192	2.981	2.095	0.396	70.209	2.903	SKKS
MMA	2007_06_13_19_29_46	52.515	2.668	0.439	0.534	19.057	45	SKS
NAA	2000_10_02_02_25_32	273.073	3.785	0.775	0.32	142.13	26.933	SKS
NOP	2007_06_13_19_29_46	53.814	2.758	1.031	0.394	166.138	10.809	SKS
NRW	2000_10_02_02_25_32	270.721	4.318	0.661	0.599	114.781	26.575	SKS
NSK	2012_05_28_05_07_23	68.169	3.239	1.907	0.698	78.697	4.408	SKKS
ONS	2000_10_02_02_25_32	274.355	2.846	1.109	0.342	128.194	14.759	SKS
SBR	2000_10_02_02_25_32	268.59	3.643	1.401	0.345	146.182	10.221	SKS
SGN	2000_10_02_02_25_32	274.108	2.77	1.374	0.465	142.93	24.676	SKS
SRN	2012_05_28_05_07_23	69.589	3.759	2.07	0.488	-0.711	4.834	SKKS
STM	2006_02_22_22_19_09	254.918	6.831	1.5	0.645	117.233	28.315	SKS
TKO	2012_05_28_05_07_23	76.51	2.981	0.695	0.407	11.748	19.365	SKKS
TSA	2000_10_02_02_25_32	269.912	5.794	0.93	0.422	128.849	26.38	SKS
TSA	2000_04_23_09_27_23	74.401	2.751	0.659	0.352	143.76	12.749	SKKS
TYS	2007_06_13_19_29_46	53.919	2.761	0.952	0.233	0.495	11.712	SKS
YZK	2012_05_28_05_07_23	69.676	3.944	0.662	0.37	122.193	29.178	SKKS

REFERENCES

Choi, H., T. K. Hong, X. He, and C. E. Baag (2012), Seismic evidence for reverse activation of a paleo-rifting system in the East Sea (Sea of Japan), *Tectonophysics*, *572*, 123-133, doi:Doi 10.1016/J.Tecto.2011.12.023.

Collings, R., A. Rietbrock, D. Lange, F. Tilmann, S. Nippress, and D. Natawidjaja (2013), Seismic anisotropy in the Sumatra subduction zone, *Journal of Geophysical Research: Solid Earth*, *118*(10), 5372-5390, doi:10.1002/jgrb.50157.

Conder, J. A., and D. A. Wiens (2007), Rapid mantle flow beneath the Tonga volcanic arc, *Earth Planet Sc Lett*, *264*(1-2), 299-307, doi:Doi 10.1016/J.Epsl.2007.10.014.

Crosweller, H. S., B. Arora, S. K. Brown, E. Cottrell, N. I. Deligne, N. O. Guerrero, L. Hobbs, K. Kiyosugi, S. C. Loughlin, and J. Lowndes (2012), Global database on large magnitude explosive volcanic eruptions (LaMEVE), *Journal of Applied Volcanology*, *1*(1), 1-13.

Crotwell, H. P., T. J. Owens, and J. Ritsema (1999), The TauP Toolkit: Flexible Seismic Travel-time and Ray-path Utilities, *Seismological Research Letters*, *70*(2), 154-160, doi:10.1785/gssrl.70.2.154.

Dziewonski, A. M., and D. L. Anderson (1981), Preliminary reference Earth model, *Phys Earth Planet In*, 25(4), 297-356.

Goldstein, P., D. Dodge, M. Firpo, and L. Minner (2003), SAC2000: Signal processing and analysis tools for seismologists and engineers, *The IASPEI International Handbook of Earthquake and Engineering Seismology*, *81*, 1613-1620.

Goldstein, P., and A. Snoke (2005), SAC availability for the IRIS community, *Incorporated Institutions for Seismology Data Management Center Electronic Newsletter*, *7*.

Hiramatsu, Y., M. Ando, and Y. Ishikawa (1997), ScS wave splitting of deep earthquakes around Japan, *Geophys J Int*, *128*(2), 409-424, doi:Doi 10.1111/J.1365-246x.1997.Tb01564.X.

Karato, S. (2003), Mapping water content in the upper mantle, *Geophysical Monograph Series*, *138*, 135-152.

Karato, S., H. Jung, I. Katayama, and P. Skemer (2008), Geodynamic significance of seismic anisotropy of the upper mantle: New insights from laboratory studies, *Annu Rev Earth Pl Sc*, *36*, 59-95, doi:Doi 10.1146/Annurev.Earth.36.031207.124120.

Kneller, E. A., M. D. Long, and P. E. van Keken (2008), Olivine fabric transitions and shear wave anisotropy in the Ryukyu subduction system, *Earth Planet Sc Lett*, *268*(3-4), 268-282, doi:Doi 10.1016/J.Epsl.2008.01.004.

Long, M. D., and P. G. Silver (2008), The subduction zone flow field from seismic anisotropy: A global view, *Science*, *319*(5861), 315-318, doi:Doi 10.1126/Science.1150809.

Long, M. D., and R. D. van der Hilst (2006), Shear wave splitting from local events beneath the Ryukyu arc: Trench-parallel anisotropy in the mantle wedge, *Phys Earth Planet In*, *155*(3-4), 300-312, doi:Doi 10.1016/J.Pepi.2006.01.003.

Long, M. D., and E. A. Wirth (2013), Mantle flow in subduction systems: The mantle wedge flow field and implications for wedge processes, *J Geophys Res-Sol Ea*, *118*(2), 583-606, doi:Doi 10.1002/Jgrb.50063.

Mahony, S. H., L. M. Wallace, M. Miyoshi, P. Villamor, R. S. J. Sparks, and T. Hasenaka (2011), Volcano-tectonic interactions during rapid plate-boundary evolution in the Kyushu region, SW Japan, *Geol Soc Am Bull*, *123*(11-12), 2201-2223, doi:Doi 10.1130/B30408.1.

Maruyama, S., Y. Isozaki, G. Kimura, and M. Terabayashi (1997), Paleogeographic maps of the Japanese Islands: Plate tectonic synthesis from 750 Ma to the present, *Isl Arc*, *6*(1), 121-142, doi:Doi 10.1111/J.1440-1738.1997.Tb00043.X.

Menke, W., and V. Levin (2003), The cross-convolution method for interpreting SKS splitting observations, with application to one and two-layer anisotropic earth models, *Geophys J Int*, 154(2), 379-392, doi:Doi 10.1046/J.1365-246x.2003.01937.X.

Nagaya, M., H. Oda, and T. Kamimoto (2011), Regional variation in shear-wave polarization anisotropy of the crust in southwest Japan as estimated by splitting analysis of Ps-converted waves on receiver functions, *Phys Earth Planet In*, *187*(1-2), 56-65, doi:Doi 10.1016/J.Pepi.2011.04.016.

Nagaya, T., S. R. Wallis, H. Kobayashi, K. Michibayashi, T. Mizukami, Y. Seto, A. Miyake, and M. Matsumoto (2014), Dehydration breakdown of antigorite and the formation of B-type olivine CPO, *Earth Planet Sc Lett*, *387*, 67-76, doi:Doi 10.1016/J.Epsl.2013.11.025.

Nozaka, T. (2005), Metamorphic history of serpentinite mylonites from the Happo ultramafic complex, central Japan, *J Metamorph Geol*, *23*(8), 711-723, doi:Doi 10.1111/J.1525-1314.2005.00605.X.

Owens, T. J., H. P. Crotwell, C. Groves, and P. Oliver-Paul (2004), SOD: Standing order for data, *Seismological Research Letters*, *75*(4), 515-520.

Plomerova, J., R. C. Liebermann, and V. Babuska (1998), Geodynamics of lithosphere and earth's mantle: Seismic anisotropy as a record of the past and present dynamic processes - Preface, *Pure Appl Geophys*, *151*(2-4), 213-219, doi:Doi 10.1007/S000240050112.

Silver, P. G. (1996), Seismic anisotropy beneath the continents: Probing the depths of geology, *Annu Rev Earth Pl Sc*, *24*, 385-432, doi:Doi 10.1146/Annurev.Earth.24.1.385.

Silver, P. G., and W. W. Chan (1991), Shear-Wave Splitting and Subcontinental Mantle Deformation, J Geophys Res-Sol Ea, 96(B10), 16429-16454, doi:Doi 10.1029/91jb00899.

Silver, P. G., and M. K. Savage (1994), The Interpretation of Shear-Wave Splitting Parameters in the Presence of 2 Anisotropic Layers, Geophys J Int, 119(3), 949-963, doi:Doi 10.1111/J.1365-246x.1994.Tb04027.X.

Tatsumi, Y., and N. Kimura (1991), Backarc Extension Versus Continental Breakup - Petrological Aspects for Active Rifting, *Tectonophysics*, *197*(2-4), 127-137, doi:Doi 10.1016/0040-1951(91)90037-S.

Uyeda, S., and A. Miyashiro (1974), Plate Tectonics and Japanese-Islands - Synthesis, *Geol Soc Am Bull*, *85*(7), 1159-1170, doi:Doi 10.1130/0016-7606(1974)85<1159:Ptatji>2.0.Co;2.

Wang, J., and D. P. Zhao (2008), P-wave anisotropic tomography beneath Northeast Japan, *Phys Earth Planet In*, *170*(1-2), 115-133, doi:Doi 10.1016/J.Pepi.2008.07.042.

Wessel, P., W. H. F. Smith, R. Scharro, J. Luis, and F. Wobbe (2013), Generic Mapping Tools: Imporved Version Released, *Eos Trans. AGU*, *94*(45), 409-410, doi:Doi: 10.1002/2013EO450001.

Wirth, E., and M. D. Long (2010), Frequency-dependent shear wave splitting beneath the Japan and Izu-Bonin subduction zones, *Phys Earth Planet In*, *181*(3-4), 141-154, doi:Doi 10.1016/J.Pepi.2010.05.006.

Wirth, E. A., and M. D. Long (2012), Multiple layers of seismic anisotropy and a low-velocity region in the mantle wedge beneath Japan: Evidence from teleseismic receiver functions, *Geochem Geophy Geosy*, *13*, doi:Artn Q08005: Doi 10.1029/2012gc004180.

Wustefeld, A., G. Bokelmann, C. Zaroli, and G. Barruol (2008), SplitLab: A shear-wave splitting environment in Matlab, *Comput Geosci-Uk*, *34*(5), 515-528, doi:Doi 10.1016/J.Cageo.2007.08.002.

CHAPTER 3

FUTURE WORK

It is clear from the results presented in Chapter 2 that the mantle wedge in Japan's subduction system is complex. Further analysis of the data is needed to better constrain the complexity of the system. Recommendations for future studies of the data to better resolve the probability of different layers of anisotropy would be to use the *Menke and Levin* [2003] approach as described below.

Menke and Levin [2003] developed a new analysis method based on *Silver and Chan* [1991] that allows for arbitrary anisotropic structures to be considered, as long as: 1) the impulse response can be modeled, and 2) the ray paths of the radial and transverse waves can be considered identical. Their method calculates cross-convolution of the observed seismic components with predicted seismic components of given splitting parameters in multilayers. They propose that if the predicted model is correct then the following will be true:

$$h_i^{pre}(m, t) * V_i^{obs}(t) \approx v_i^{pre}(m, t) * H_i^{obs}(t)$$

where h_i^{pre} is the predicted radial impulse response function, V_i^{obs} is the observed tangential horizontal seismogram, v_i^{pre} is the predicted tangential impulse response function, and H_i^{obs} is the radial seismogram [*Menke and Levin*, 2003].

An advantage of this technique is that complex layering of anisotropy can be tested, as long as the anisotropic impulse response can be computed. Unlike *Silver and Chan's* [1991] technique that assumes a single layer of anisotropy exists, this modeling technique allows for multiple layers of anisotropy to be tested [*Menke and Levin*, 2003]. A study done by *Wirth and Long* [2012] suggests that there are multiple layers of anisotropy beneath Japan; therefore, *Menke and Levin's* [2003] could better resolve the complexity of the data that was seen in the "Good Events" results.

REFERENCES

Menke, W., and V. Levin (2003), The cross-convolution method for interpreting SKS splitting observations, with application to one and two-layer anisotropic earth models, *Geophys J Int*, *154*(2), 379-392, doi:Doi 10.1046/J.1365-246x.2003.01937.X.

Silver, P. G., and W. W. Chan (1991), Shear-Wave Splitting and Subcontinental Mantle Deformation, *J Geophys Res-Sol Ea*, *96*(B10), 16429-16454, doi:Doi 10.1029/91jb00899.

Wirth, E. A., and M. D. Long (2012), Multiple layers of seismic anisotropy and a low-velocity region in the mantle wedge beneath Japan: Evidence from teleseismic receiver functions, *Geochem Geophy Geosy*, *13*, doi:Artn Q08005: Doi 10.1029/2012gc004180.